

Aberrant levels of histone H3 acetylation induce spermatid anomaly in mouse testis

Lei Dai, Daisuke Endo, Naotaro Akiyama, Tomomi Yamamoto-Fukuda,
Takehiko Koji

Department of Histology and Cell Biology, Nagasaki University Graduate
School of Biomedical Sciences, 1-12-4 Sakamoto, Nagasaki 852-8523, Japan

Correspondence:

Takehiko Koji, Department of Histology and Cell Biology, Nagasaki
University Graduate School of Biomedical Sciences, 1-12-4 Sakamoto,
Nagasaki 852-8523, Japan.

Email: tkoji@nagasaki-u.ac.jp

Phone: +81 95-819-7025

Fax: +81 95-819-7028

Abstract

Histone acetylation is involved in the regulation of chromatin structure and gene function. We reported previously that histone H3 acetylation pattern is subject to dynamic changes and limited to certain stages of germ cell differentiation during murine spermatogenesis, suggesting a crucial role for acetylation in the process. In the present study, we investigated the effects of hyper- and hypo-acetylation on spermatogenesis. Changes in acetylation level were induced by either *in vivo* administration of sodium phenylbutyrate, a histone deacetylase inhibitor, or by knockdown of histone acetyltransferases using short hairpin RNA plasmids transfection. Administration of sodium phenylbutyrate induced accumulation of acetylated histone H3 at lysine 9 and lysine 18 in round spermatids, together with spermatid morphological abnormalities and induction of apoptosis through a Bax-related pathway. Knockdown of steroid receptor coactivator 1, a member of histone acetyltransferases, but not general control of amino-acid synthesis 5 nor elongator protein 3 by *in vivo* electroporation of shRNA plasmids, reduced acetylated histone H3 at lysine 9 in round spermatids, and induced morphological abnormalities. We concluded that the proper regulation of histone H3 acetylation levels is important for spermatid differentiation and complex chromatin remodeling during spermiogenesis.

Keywords: Histone H3, Acetylation, Abnormal morphology, Apoptosis, Round spermatid, Murine spermatogenesis

Introduction

Post-translational modifications of histones are associated with distinct transcription states and serve as heritable epigenetic markers for chromatin structure and function (Berger 2002). Among the modifications, acetylation of lysine residues is well characterized and known to be as a trigger for chromatin reorganization, remodeling and affects gene expression (Natsume-Kitatani et al. 2011). Generally, histone acetylation is associated with gene transcription while histone deacetylation is coupled to gene silencing (Kuo and Allis 1998). Acetylation of histone H3 occurs at several different lysine residues in the histone tail, and is a key element in the dynamic regulation of genes controlling cellular proliferation, differentiation and apoptosis (Suka et al. 2001; Vempati et al. 2010). It has been reported that conversion from methylation to acetylation of histone H3 at lysine 9 changes heterochromatin to euchromatin, with subsequent recruitment of transcriptional complexes to genes for transactivation (Kondo et al. 2004).

Mammalian spermatogenesis is a unique process with successive proliferation and differentiation, consisting of spermatogonial self-renewal, spermatocytic meiosis and spermiogenic chromatin remodeling (Roosen-Runge 1962). Therefore, we selected spermatogenesis as a model system to investigate the roles of histone acetylation on such biological processes, including cell proliferation, differentiation, and chromatin organization. Recent studies in mice have demonstrated the occurrence of waves of histone acetylation throughout spermatogenesis (Govin et al. 2006; Song et al. 2011). Global hyperacetylation of core histones, especially histone H4, is known to play an important role in the histone-to-protamine exchange during spermiogenesis (Hazzouri et al. 2000). However, less attention has been given to the potential role of histone H3 in spermatogenesis. In our previous study (Song et al. 2011), we found that during mouse spermatogenesis, the acetylated histone H3 at lysine 9

(H3K9ac), lysine 18 (H3K18ac) and lysine (H3K23ac), are subjected to dynamic changes specifically at certain stage of germ cell differentiation. Hyperacetylation of H3K9, H3K18 and H3K23 was observed in spermatogonia, and then reduced in pachytene spermatocytes. In the ensuing spermiogenesis, histone H3 was hypoacetylated at K9, K18 and K23 in step 1-8 round spermatids, then re-acetylated and reached a peak in elongated spermatids around step 9, followed by a loss after step 13. Recently, it also has been reported that mutation of chromatin remodeling protein, pygopus homolog 2 (PYGO2) (Nair et al. 2008) and inhibitor of growth family member 2 (ING2) (Saito et al. 2010) caused defects of spermatogenesis and aberrant histone H3 modification patterns in spermatogenic cells. Therefore, we hypothesized these modifications are important in the regulation of murine spermatogenesis.

Acetylation of core nucleosomal histones is a reversible process controlled by two classes of enzymes, histone acetyltransferases (HATs) and histone deacetylases (HDACs) (Kuo and Allis 1998). Several HAT proteins have been identified in various organisms, and are grouped into five families, including the amino-acid synthesis 5 (GCN5)-related N-terminal acetyltransferases family such as GCN5 and elongator protein 3 (ELP3) (Neuwald and Landsman 1997; Wittschieben et al. 1999), the MYST family (Neal et al. 2000), the p300/cAMP-response element binding (CREB) protein family (Giles et al. 1998), the general transcription factor family (Mizzen et al. 1996) and the nuclear hormone-related family (Spencer et al. 1997). Steroid receptor coactivator 1 (SRC-1) as a member of the nuclear hormone-related HATs, possess histone acetyltransferase activity for histone H3 at some specific residues. SRC-1 may facilitate specific gene transcription through targeted histone acetylation, resulting in localized chromatin remodeling and recruitment of the pre-initiation complex (Spencer et al. 1997).

On the other hand, in mammals, 18 HDACs have been identified so far, which are grouped into Class I, Class II, and Class III (de Ruijter et al. 2003). Among various histone deacetylase inhibitors (HDACis), sodium phenylbutyrate (NaPB) is a non-toxic Class I/II HDACi that has been approved for treatment of urea cycle disorders by U.S. Food and Drug Administration and is currently being tested for the treatment of cancer, hemoglobinopathies, motor neuron diseases, and cystic fibrosis (Lee et al. 2010; Iannitti and Palmieri 2011). NaPB causes cellular differentiation, growth arrest, and apoptosis of transformed cells or cancer cells, such as colon carcinoma, prostate cancer, primary acute myeloid leukemia, retinoblastoma and lung carcinoma cells (Feinman et al. 2002; Milkevitch et al. 2005; Yu et al. 1999; Calvaruso et al. 2001; Boivin et al. 2002).

The present study was designed to determine the effects of manipulation of histone H3 acetylation on mouse spermatogenesis through changes in the HDAC/HATs balance by *in vivo* NaPB treatment or knockdown of HATs by *in vivo* electroporation of shRNA plasmids. Using various morphological and histochemical approaches, we found that manipulation of histone H3 acetylation induced morphological abnormalities and apoptosis of round spermatids during spermatogenesis.

Materials and methods:

Chemicals and biochemicals

NaPB, bovine serum albumin (BSA), dimethyl sulfoxide (DMSO), proteinase K, Brij 35 and 3-aminopropyltriethoxysilane (APS) were from Sigma-Aldrich (St. Louis, MO, USA). Suberoylanilide hydroxamic acid (SAHA) was from Cayman Chemical (Ann Arbor, MI, USA). Somnopentyl was from Kyoritsu Seiyaku Corp (Tokyo, Japan). Paraformaldehyde (PFA) was from Merck (Darmstadt, Germany). 3, 3'-Diaminobenzidine-4 HCl (DAB) was from Dojindo Chemicals (Kumamoto, Japan).

Biotin-16-dUTP, digoxigenin-11-dUTP and terminal deoxynucleotidyl transferase (TdT) were from Roche Diagnostics (Mannheim, Germany). Dideoxy-ATP (ddATP) and dideoxy-TTP (ddTTP) were from Jena Bioscience (Jena, Germany). *HpaII* and *MspI* were from Takara Bio Inc. (Shiga, Japan). 4',6-Diamidino-2-phenylindole dihydrochloride (DAPI) was from DAKO (Glostrup, Denmark). Permunt was from Thermo Fisher Scientific (Hudson, NH, USA). Epon 821 was from Taab Lab (Aldermaston, Berkshire, UK). All other reagents used in this study were from Wako Pure Chemicals (Osaka, Japan) and were of high analytical grade.

Antibodies

Rabbit polyclonal anti-H3K9ac (1:50 dilution; product no.9671), anti-H3K18ac (1:100 dilution; product no.9675), anti-H3K23ac (1:25 dilution; product no.8848) and rabbit monoclonal anti-SRC-1 (1:100 dilution; product no.2191) antibodies were from Cell Signaling Technology (Beverly, MA, USA). Rabbit polyclonal anti-Bax (1:100 dilution; product no.sc-526) and anti-Bcl-2 (1:100 dilution; product no.sc-492) antibodies were from Santa Cruz Biotechnology (Santa Cruz, CA, USA). Mouse monoclonal anti-8-hydroxy-2'-deoxyguanosine (8-OHdG) (1:50; product no.MOG-020P) antibody was from Japan Institute for the Control of Aging (Shizuoka, Japan). Rabbit polyclonal anti-5-hydroxymethylcytosine (5hmC) (1:500 dilution; product no.39769) antibody was from Active Motif (Carlsbad, CA, USA). Mouse monoclonal anti-5-methylcytosine (5mC) (1:400 dilution; product no.NA81) antibody was from Calbiochem (San Diego, CA, USA). Rabbit polyclonal anti-Elp3 (1:100 dilution; product no.ab113228) and Mouse monoclonal anti-DNA methyltransferase 1 (Dnmt1) (1:250 dilution; product no.ab92453) antibodies were from Abcam (Cambridge, MA, USA). Rabbit polyclonal anti-GCN5 (1:100 dilution; product no.NBP1-00845) antibody was from Novus Biologicals (Littleton,

CO, USA). Mouse polyclonal anti-green fluorescent protein (GFP) (1:200 dilution; product no.M048) antibody was from MBL (Nagoya, Japan). Horseradish peroxidase (HRP)-goat anti-mouse IgG (1:100 dilution; product no.AP181P) and HRP-goat anti-rabbit IgG (1:100 dilution; product no.AP307P) antibodies were from Millipore (Temecula, CA, USA). FITC-labeled goat anti-biotin (1:100 dilution; product no.SP-3040) and HRP-goat anti-biotin (1:100 dilution; product no.SP-3010) antibodies were from Vector Laboratories (Burlingame, CA, USA). Rhodamine-labeled sheep anti-digoxigenin (1:100 dilution; product no.11207750910) antibody was from Roche Diagnostics. Alexa Fluor 488-goat anti-mouse IgG (1:500 dilution; product no.A11017) and Alexa Fluor 546-goat anti-rabbit IgG (1:500 dilution; product no.A11071) antibodies were from Thermo Fisher Scientific. Normal goat IgG and sheep IgG were from Sigma-Aldrich. Normal mouse and rabbit IgG were from DAKO.

Animals

Adult (7 to 8-week-old, 30–35 g body weight) and neonatal (18-day-old, 8-11 g body weight) male ICR mice were used in the present study. All experiments were conducted according to the principles and procedures outlined in the guidelines for animal experimentation of Nagasaki University with the approval of the institutional Animal Care and Use Committee (#1004010843).

Treatment with NaPB

Adult male ICR mice were used for HDACi treatment. NaPB which dissolved in phosphate-buffered saline (PBS, pH 7.4) was administered intraperitoneally once at a dose of 800 mg/kg body weight.

Control animals were treated with an equivalent volume of PBS instead of NaPB (Petri et al. 2006). We also treated the mice by once intraperitoneal injection of another HDACi SAHA which dissolved in

DMSO at the dose of 150 mg/kg body weight. Control animals were treated with an equivalent volume of DMSO instead of SAHA.

Construction of mU6-HAT shRNA-SV40-GFP plasmids

SRC-1, GCN5 and ELP3 which acetylated histone H3 were selected as target genes for knockdown experiment. Coding sequences for mouse SRC-1 (MGI:1276523), GCN5 (MGI:1343101) and ELP3 (MGI:1921445) were targeted by 21mer short hairpin RNA (shRNA) sequences designed using the BLOCK-iT RNAi Designer (Thermo Fisher Scientific) (Meister and Tuschl 2004). The obtained target sequences, (SRC-1-2741) 5'- GGAGGTACTTGTCCCTCTTCT-3', (GCN5-657) 5'-GCTCTTGCGGAAGTGCATTCT-3' and (ELP3-1052) 5'-GGTTTGAAGCTCTACCCAACC-3' were at least four mismatches with other genes in mouse genome as determined by a Blast analysis. The sequences were used to generate oligo-nucleotides targeting SRC-1, GCN5 and ELP3. The oligonucleotides were inserted into the pRNAi-mU6-green plasmid (Biosettia, San Diego, CA, USA), which has co-cistronic expression of GFP, allowing for the determination of transfection efficiency by fluorescence microscopy. The shRNA expression plasmids targeting the SRC-1 gene (designated SRC-1-shRNA plasmid), GCN5 gene (designated GCN5-shRNA plasmid) and ELP3 gene (designated ELP3-shRNA plasmid) were sequence-verified. The mU6-LacZ shRNA-SV40-green plasmid contains an oligonucleotide targeting lacZ, which served as a negative control (designated LacZ-shRNA plasmid).

In vivo electroporation

The neonatal male ICR mice were used for *in vivo* electroporation. Plasmids for injection were

dissolved in PBS at 600 $\mu\text{g}/\text{ml}$ with 0.04% trypan blue to monitor needle positioning and injection accuracy. The mice were anesthetized by intraperitoneal injection of Somnopentyl (50 mg/kg body weight) before the surgery, and then the abdominal cavity was opened. Approximately 10-15 μl of plasmid solution was directly injected into 18-day-old mouse testes using electrosyringe (Altair Co, Kanagawa, Japan). The right testis was injected with HATs shRNA plasmids (SCR-1-, GCN5- or ELP3-shRNA plasmids), and the left testis was injected with the control plasmids (LacZ-shRNA plasmids). Electric pulses were generated with an electroporator NEPA21 type II (NEPA GENE Co, Chiba, Japan). Testes were held between a pair of tweezer-type electrodes (NEPA GENE), and square electric pulses were applied at the condition of 8 square 50 V electric pulses in alternating direction with a time constant of 0.05 s and an inter-pulse interval of 0.95 s (Yomogida et al. 2002). After surgery, the abdominal muscle and the skin were carefully closed with suture.

Tissue preparation

For treatment with NaPB or SAHA as HDACis, the adult male mice were sacrificed at 3, 6, 12, 24 h after the injection (Petri et al. 2006). For *in vivo* electroporation with shRNA plasmids, the 18-day neonatal male mice were sacrificed at 10 days after transfection. One testis of each adult mouse with HDACi treatment was fixed overnight with 4% PFA and 2% glutaraldehyde in 0.1 M cacodylate buffer (pH 7.4), then processed routinely and embedded in Epon 821. The other testis of adult mouse for HDACi treatment and the testes of electroporated neonatal mice were fixed overnight with 4% PFA in 0.01 M PBS and embedded in paraffin according to the standard procedures. Postnatal and adult mice were killed by cervical dislocation, and the testes were collected and processed as described above. Transfected testes were observed and photographed using a Leica MZ16F fluorescent

stereomicroscopy with Leica DFC300 FX digital camera (Leica Microscopy System Ltd., Wetzlar, Germany) after collection. The paraffin-embedded testes were cut into 5 μm -thick sections and mounted onto APS-precoated slides. For histological examination, some sections were stained with hematoxylin and eosin (H&E). Unless otherwise specified, all procedures were performed at room temperature (RT).

Electron microscopy (EM)

Epon-embedded testes were cut into semithin and ultrathin sections. The semithin sections were stained with toluidine blue, and the ultrathin sections were stained with uranium acetate and lead nitrate. The ultrathin sections were observed under a JEOL 1200EX electron microscopy (JEOL, Peabody, MA, USA) at accelerated voltage of 60 kV as described previously (Wang et al. 1998).

Immunohistochemistry

Immunohistochemical staining was performed by the indirect enzyme-labeled antibody method, as described previously (Damavandi et al. 2002; Song et al. 2011). Briefly, paraffin-embedded testes sections were deparaffinized with toluene and rehydrated with serial graded ethanol solutions. Except for Bcl-2 and 8-OHdG, the sections were then autoclaved at 120 °C for 15 min in 10 mM citrate buffer (pH 6.0). Then, the sections were preincubated with 500 $\mu\text{g/ml}$ normal goat IgG dissolved in 1% BSA in PBS for 1 h. Then, the sections were reacted with the primary antibodies for 16 h. After washing with 0.075% Brij 35 in PBS, they were reacted with HRP-goat anti-mouse IgG or HRP-goat anti-rabbit IgG for 1 h. After washing in 0.075% Brij 35 in PBS, the HRP sites were visualized as described above. For double immunofluorescence staining, the sections were incubated with Alexa Fluor 488-goat

anti-mouse IgG and Alexa Fluor 546-goat anti-rabbit IgG for 1 h. After 3 times washing with 0.075% Brij 35 in PBS, the sections were counterstained with DAPI. As a negative control, normal mouse or rabbit IgG was used at the same concentration instead of the primary antibodies in every experiment.

Terminal deoxynucleotidyl transferase dUTP nick end labeling (TUNEL) staining

To identify apoptotic germ cells, TUNEL was performed according to the method as described previously (Gavrieli et al. 1992) with a slight modification. Paraffin sections were dewaxed and digested with 10 µg/ml of proteinase K in PBS at 37 °C for 15 min. Then the sections were reacted with 1×TdT buffer (825 mM Tris/HCl buffer, pH 6.6, containing 0.2 M potassium cacodylate and 0.25 mg/ml BSA) alone at RT for 30 min. After the incubation, the slides were reacted with 800 units/ml TdT dissolved in TdT buffer supplemented with 0.5 µM biotin-16-dUTP, 20 µM dATP, 1.5 mM CoCl₂, and 0.1 mM dithiothreitol at 37 °C for 90 min. As a negative control, TdT reaction was conducted without TdT. After washing with milli-Q water (Millipore, Molsheim, France) (DDW), the signals were detected immunohistochemically with HRP-goat anti-biotin antibody. The sites of HRP were visualized by a mixture of DAB, hydrogen peroxide, nickel and cobalt ions, as described above. For immunofluorescence staining, the sections were incubated with FITC-labeled goat anti-biotin antibody for 1 h. After 3 times washing with 0.075% Brij 35 in PBS, the sections were counterstained with DAPI.

In situ evaluation of DNA methylation

To evaluate the DNA methylation level of the testes sections of NaPB and PBS treated mice at CCGG sites, histo-endonuclease-linked detection of methylation sites of DNA (HELMET) was performed

(Koji et al. 2008). First, to block the free 3'-OH ends of DNA which may occur in the tissue processing and cell death, TdT reaction was conducted as described above on paraffin sections of mouse testis at 37 °C for 2 h, except for the presence of 20 µM ddATP and 20 µM ddTTP instead of dATP and biotin-16-dUTP. After washing with DDW and PBS, successively, the sections were fixed with 4% PFA in PBS for 5 min and then washed twice with PBS and once with DDW for 5 min each. The non-methylated CCGG sites were digested with 100 units/ml of *HpaII*, dissolved in 10 mM Tris/HCl buffer (pH 7.5), containing 10 mM MgCl₂ and 1 mM dithiothreitol at 37 °C for 2 h. The *HpaII*-cut sites were labeled with biotin-16-dUTP by TdT reaction at 37 °C for 1.5 h in a moist chamber. Then the free 3'-OH ends were blocked with a mixture of dideoxynucleotides by TdT, as described above, for 2 h at 37 °C. After fixation with 4% PFA in PBS, the methylated CCGG sites were digested at 37 °C for 2 h by 100 units/ml *MspI*, dissolved in Tris/HCl buffer (pH 7.9), containing 10 mM MgCl₂, 0.5 mM dithiothreitol, 66 mM potassium acetate and 0.1% BSA at 37 °C for 2 h. The *MspI*-cut sites were then labeled with digoxigenin-11-dUTP by TdT reaction for 1.5 h at 37 °C in a moist chamber. Finally, the sections were incubated with a mixture of 500 µg/ml normal goat IgG and normal sheep IgG in 5% BSA/PBS for 1 h, and then visualized by FITC-goat anti-biotin and rhodamine-sheep anti-digoxigenin antibodies. The nuclei were stained with 0.5 µg/ml DAPI for 1 min. In this study, FITC and rhodamine signals were obtained with an emission of 505–530 nm (excitation; 488 nm) and ~560 nm filter (excitation; 543 nm), respectively. The observation was done with Plan-NeoXuar 40×/0.75 objective lenses. All microscope settings were set to collect images below saturation and were kept constant for all images taken in each sample. To avoid technical errors among different samples, round spermatids were used as an internal control in PBS and NaPB-treated testes. The analysis of fluorescence signals was performed with LSM 5 Pascal (V3.2) (Carl Zeiss Co., Jena, Germany). Nuclei were defined using

the DAPI channel, and mean (total/number of pixels) intensities within this region were recorded for the each fluorophores. And then the global methylation intensities were calculated as the ratio of rhodamine /FITC for each nucleus.

Statistical analysis

TUNEL-positive cells were counted as apoptotic cells by examining 100-200 of round seminiferous tubules in each group, and the frequency was finally expressed as the number of apoptotic germ cells per 100 tubules. The fluorescence intensity was measured on a minimum of 100 cells for each sample from the fluorescence image. All data were expressed as mean \pm SD. Statistical significance was assessed by Student's *t*-test. $P < 0.05$ was considered statistically significant. All analyses were performed with the Statistical Package for the Social Sciences (Version 13.0; Chicago, IL, USA).

Results

Histological changes in mouse testes at various time-points after NaPB treatment

Histological examination of the testes of NaPB-treated mice showed morphologically abnormal round spermatids characterized by detachment or sloughing into the lumen of the seminiferous tubules and formation of round spermatid aggregates at 6 h after treatment (Fig. 1). Tubules displaying abnormal histology were mainly found at stage I-VII (Fig. 1e, f). Abnormal features were observed in the newly formed round spermatids at stage XII-I (e' in Fig. 1e) as well as pre-existing round spermatids at stage II-VII (f' in Fig. 1f). However, the other germ cells such as spermatogonia, spermatocytes and elongated spermatids appeared normal and unaffected during the treatment course. The above changes were markedly attenuated at 12 h after NaPB treatment and the normal features reappeared at 24 h after

the treatment. For SAHA treatment, massive apoptosis occurred in pachytene spermatocytes at 12 h after treatment (Fig. S1e, f) without any effects on other germ cells.

Acetylation levels of histone H3 after NaPB treatment

Members of the HDAC deacetylate histones (Kuo and Allis 1998). To examine the effects of NaPB on acetylated histone H3, we used immunohistochemistry to investigate the expression of histone H3K9ac, H3K18ac and H3K23ac in paraffin sections of NaPB-treated testes (Fig. 2). In the control PBS-treated testes, relatively low level of histone H3 acetylation was noted at Lys 9, 18 and 23 among step 1-7 spermatids (Fig. 2b-d). Treatment with NaPB markedly increased H3K9ac (Fig. 2g) and H3K18ac (Fig. 2h) levels in the round spermatid aggregates (arrows in Fig. 2g, h) at 6 h after the treatment. However, treatment with NaPB did not affect H3K23ac level so much (Fig. 2i). Further, the same treatment had no effect on other spermatogenic cells as well as Sertoli and Leydig cells. For SAHA treatment, however, there was no apparent change in the level of histone H3 acetylation in apoptotic pachytene spermatocytes and any other germ cells (Fig. S2).

Induction of apoptosis in round spermatids by NaPB treatment

The weight of testes of NaPB-treated mice at 12 h after treatment was about 30% lower than that of the control group (Fig. 3a). In the next step, we applied TUNEL staining using paraffin-embedded sections to assess the effect of NaPB on apoptosis of germ cells (Fig. 3b-f). In testes of the control mice, TUNEL-positive cells formed about 20 per 100 seminiferous tubules at all time-points. This rate was similar to that found in mice of the no-treatment group (Fig. 3b). In NaPB-treated testes, the number of apoptotic cells at 3 h after the treatment showed almost no change (Fig. 3b). As shown in Fig. 3b and f,

the percentage of apoptotic cells was significantly increased and reached maximum at 6 h after treatment with NaPB, and the apoptotic cells were almost all in sloughing spermatid aggregates (arrowheads in Fig. 3f). However, the number of apoptotic cells decreased at 12 and 24 h after the treatment, consistent with the morphological recovery described above (Fig. 3b). To confirm that these results were not caused by toxic effects of high dose treatment of NaPB, we performed TUNEL and immunohistochemistry for reactive oxygen species (ROS) marker, 8-OHdG using the paraffin sections of NaPB and SAHA treated testes (Fig. S1). TUNEL positive-pachytene spermatocytes of SAHA treated testes were positive for 8-OHdG (arrows in Fig. S1f, g), whereas apoptotic round spermatids were negative for 8-OHdG in NaPB treated testes (arrowheads in Fig. S1b, c).

Electron microscopic analysis of abnormal round spermatid aggregates after NaPB treatment

To further characterize the abnormal round spermatids, we analyzed the aggregates by electron microscopy (Fig. 4). The round spermatids in such aggregates sometimes showed multinucleated syncytium formation (Fig. 4b), together with cell membrane fusion (asterisk in Fig. 4b).

NaPB up-regulates Bax and down-regulates Bcl-2 expression

In the next step, we investigated the mechanism of NaPB-induced apoptosis by immunohistochemistry, with a special focus on Bcl-2/Bax system based on its known involvement in germ cell apoptosis (Damavandi et al. 2002). Strong cytoplasmic staining for proapoptotic protein Bax was observed in the round spermatid aggregates at 6 h after NaPB treatment (d' in Fig. 5d), but not in the testes of PBS-treated mice (Fig. 5c). On the other hand, the anti-apoptotic protein Bcl-2 was expressed very weakly in the round spermatid aggregates of NaPB-treated mice (g' in Fig. 5g), while such staining was

intense in the cytoplasm of round spermatids of PBS-treated mice (Fig. 5f).

NaPB induces global demethylation of CCGG sites in round spermatid aggregates

Histone H3 acetylation is dynamically and physically linked to DNA methylation, and H3K9ac correlate negatively with DNA methylation levels (Zhang et al. 2012). Based on this background, we evaluated the DNA methylation level at CCGG sites in NaPB- and PBS-treated testes at 6 h after treatment by HELMET. The staining of both non-methylated (Fig. 6e) and methylated CCGG sites (Fig. 6f) were generally stronger in the round spermatid aggregates of NaPB-treated testes at 6 h after treatment, compared with PBS-treated testes. However, the global CCGG methylation, represented by the ratio of methylated CCGG/non-methylated CCGG, was 30% lower in the round spermatid aggregates of NaPB-treated testes ($P < 0.05$) (Fig. 6 g' and i), than their counterparts of PBS-treated testes (Fig. 6 c' and i).

NaPB induces demethylation of DNA and reduces nuclear Dnmt1 in round spermatid aggregates

To confirm the finding of demethylation in CCGG sites of round spermatid aggregates of NaPB-treated mice, we used immunohistochemistry to determine the expression levels of 5mC and 5hmC in NaPB-treated testes at 6 h after the treatment. The round spermatids of PBS-treated mice stained strongly for 5mC (Fig. 7b), but were negative for 5hmC (Fig. 7c). On the other hand, the round spermatids of the aggregates of NaPB-treated mice stained weakly for 5mC (arrowheads and g' in Fig. 7g), and positively for 5hmC (arrows and h' in Fig. 7h). To gain insight into the possible mechanisms of NaPB-induced DNA demethylation in the round spermatids, we used immunohistochemistry to determine the expression of Dnmt1 (Fig. 7d, i). Immunostaining for Dnmt1 was markedly lowered in

round spermatid aggregates of NaPB-treated testes (open arrows and i' in Fig. 7i).

NaPB-induced DNA demethylation correlates with induction of apoptosis in round spermatid aggregates

As shown in Fig. 8, in experiments involving double staining for TUNEL (Fig. 8a) and HELMET with *HpaII* (Fig. 8b), TUNEL-positive round spermatids were always strongly positive for non-methylated CCGG (arrows), but not all of round spermatids with elevated non-methylated CCGG signals were TUNEL-positive (arrowheads).

Changes in HAT expression after in vivo shRNA plasmid transfection by electroporation

In the first series of these experiments, we confirmed the stable expression of shRNA plasmids electroporated into germ cells over a long period of time. GFP was detected in all transfected testes at day 10 after electroporation (Fig. 9a) whereas no GFP positive cells were observed in non-transfected testes at the same age (Fig. S3). To assess the knockdown efficiency on HATs after transfection, we investigated the expression levels of SRC-1, GCN5 and ELP3 in GFP-positive cells of the corresponding transfected testes. As shown in Fig 9, the SRC-1 level in GFP-positive round spermatids of SRC-1-shRNA transfected testes (arrowhead and f' in Fig. 9f) was significantly lower than that of the control testes (arrow and c' in Fig. 9c). In GCN5- and ELP3-shRNA transfected testes, the GCN5 and ELP3 levels in GFP-positive cells were also markedly lower after transfection (Fig. S4 and S5).

Acetylated histone H3 levels after knockdown of HATs by shRNA plasmid transfection

To investigate the effect of HATs knockdown on histone H3 acetylation level, we examined the levels of histone H3K9ac, H3K18ac and H3K23ac after transfection. H3K18ac and H3K23ac levels were not apparently affected in any of the transfected testes (Fig. S6). The H3K9ac level in GFP-positive round spermatids of SRC-1-shRNA transfected testes (arrowheads; Fig. 10c-e) was about 35% lower than that of the control (arrows; Fig. 10a, b, e). However, the H3K9ac level was not significantly reduced in GFP-positive round spermatids of GCN5- and ELP3-shRNA transfected testes (Fig. S6).

Induction of apoptosis in round spermatids by SRC-1-shRNA plasmid transfection

TUNEL was carried out on paraffin sections of the transfected testes at day 10 post transfection (Fig. 11). The proportion of TUNEL-positive cells relative to the total testicular cells was not significantly different between transfected testes (data not shown). However, the number of apoptotic round spermatids was significantly higher in SRC-1-shRNA transfected testes compared with control testes (arrowheads in Fig. 11d and Fig. 11e).

Discussion

To determine the role of acetylated histone H3 in mouse spermatogenesis, we examined the effects of up- and down-regulation of histone H3 acetylation on the morphological changes in spermatogenic cells through HDAC inhibition and HATs knockdown, respectively. Our results demonstrated for the first time that aberrations in the state of histone H3 acetylation can induce morphological abnormalities and apoptosis of round spermatids. These results suggest that acetylated histone H3 plays a crucial role in the regulation of round spermatid differentiation during spermiogenesis. In addition, we presented evidence for the coordination of epigenetic parameters (e.g.,

hyperacetylation of histones and demethylation of DNA) in round spermatids.

Histone acetylation occurs at various lysine residues. It has been shown that specific residues on the histone tails can be modified and that a specific pattern of histone modification is involved in the regulation of gene transcriptional activity (Munshi et al. 2009). More importantly, the states of acetylation are not fixed, rather changeable (Hazzouri et al. 2000; Song et al. 2011). In our previous study (Song et al. 2011), hyperacetylation of histone H3 at K9, K18 and K23, was detected in the nuclei of spermatogonia and preleptotene spermatocytes. Interestingly, the acetylation level decreased until round spermatid formation (steps 1-7), but re-acetylation occurred around step 8 in the elongated spermatids in mouse testes.

In the present study, NaPB remarkably increased histone H3K9ac and H3K18ac levels in round spermatids (steps 1-7). In contrast, histone H3 acetylation level did not change in any other types of germ and somatic cells, as assessed by quantitative immunohistochemistry. These results suggest the importance of HDAC activity in maintaining a state of histone H3 hypoacetylation in round spermatids, and lack of its role in the control of acetylation level in other types of germ cells.

Our morphological studies demonstrated the generation of detaching or sloughing round spermatid aggregates, sometimes multinucleated syncytia of round spermatids following treatment with NaPB. The presence of these round spermatids suggests failure of mechanisms that normally maintain the adhesion of round spermatids and Sertoli cells. In this regard, N-cadherin is considered a cell adhesion molecule actively engaged in spermatid-Sertoli cell adhesion (Kopera et al. 2010), and its expression in tumor cells is reduced following treatment with HDACi (Shah et al. 2014). On the other hand, inactivation of HDAC6, a tubulin deacetylase known to be specifically upregulated in the testis compared with other tissues (Zhang et al. 2008), may also be involved in round spermatid detachment.

In this context, it should be noted that loss of Sertoli cell function often leads to the formation of similar multinucleated syncytia (Creasy et al. 1990). However, this would not be the case because no apparent changes in histone H3 acetylation level and morphology were identified in the present study.

NaPB induced global demethylation of CCGG sites in round spermatid aggregates, as identified by HELMET, but it increased the numbers of both non-methylated and methylated CCGG sites. It was not caused by the detection of 3'-OH ends of DNA that were generated during the process of apoptosis, because these free ends were completely blocked with dideoxynucleotides by TdT reaction (arrows in Fig. S7). The above results were expected because NaPB-induced histone H3 hyperacetylation may trigger the conversion of heterochromatin to euchromatin, with subsequent recruitment of the isochizomer restriction enzymes; *HpaII* and *MspI*, for more efficient digestion of DNA sites in the original heterochromatin area.

Clearly, demethylation in aggregated round spermatids was not related to replication, since no DNA synthesis was noted in round spermatids. We have demonstrated that not all round spermatids with demethylated CCGG sites were TUNEL positive (Fig. 8 and Fig. S7). This indicated that the global demethylation of DNA in round spermatids after NaPB treatment were not downstream events of apoptotic process. It has been reported that HDACi promotes ubiquitin-dependent proteasomal degradation of Dnmt1 in cancer cells (Zhou et al. 2008). Our results of NaPB-induced reduction of nuclear Dnmt1 add support to the above studies. Moreover, histone hyperacetylation has been found to enhance the activity of methylated DNA-binding protein 2/DNA demethylase (MBD2/dMTase) (Cervoni and Szyf 2001; Detich et al. 2003). Considered together, we believe that Dnmt1 degradation and demethylase activation by histone H3 hyperacetylation are the underlying mechanisms of NaPB-induced demethylation in aggregated round spermatids.

Why were the round spermatids specifically targeted for apoptosis by NaPB? Accumulation of ROS is a potential mechanism underlying HDACi lethality in transformed cells exposed to structurally diverse HDACis, including SAHA, TSA and sodium butyrate (Ruefli et al. 2001; Ungerstedt et al. 2005; Louis et al. 2004). But in the previous study using a mouse model of Parkinson's disease, NaPB protected dopaminergic neurons, suggesting it has antioxidant activity (Roy et al. 2012). Consistent with those of previous studies, we have demonstrated that 8-OHdG, one marker of oxidative stress cannot be detected in the NaPB treated testes which was positive in SAHA induced apoptotic spermatocytes (Fig. S1). It is already known that SAHA induces the expression of thioredoxin-binding protein-2 through the activation of NF- κ B. This protein suppresses the expression of thioredoxin and causes the production of ROS (Butler et al. 2002). On the other hand, the previous studies have indicated that the exposure of tumor cells to NaPB leads to inactivation of NF- κ B (Feinman et al. 2002). Thus, it is possible that the apoptosis induced by SAHA may be due to the side effect of ROS, because no apparent changes were found in histone H3 acetylation (Fig. S2) and ROS was accumulated in apoptotic pachytene spermatocytes (Fig. S1). It has been already reported that NF- κ B p50 and p65 subunits are transiently expressed in the nuclei of germ cells with peak levels found in pachytene spermatocytes and low levels in round spermatids (Delfino and Walker 1998). This may explain that accumulation of ROS and induction of apoptosis were observed predominantly in pachytene spermatocytes of SAHA-treated testes. Based on the above results, one can rule out any role for ROS in triggering round spermatid apoptosis. Considering that histone H3 hyperacetylation and global DNA demethylation in aggregated round spermatids are typical effects of NaPB treatment, disorders of epigenetic regulation could be involved in the induction of apoptosis of round spermatids.

How does the epigenetic disorder affect round spermatid gene expression? There are at least 348

haploid genes with similar stage-specific expression patterns; the expression begins in round spermatids between steps 1 and 6, and increases gradually, reaching a maximum in steps 8–12 spermatids (Penttila et al. 1995; Lin and Matzuk 2005). The importance of the balance between transcriptional activation and repression is well demonstrated in normal spatiotemporal haploid gene expression, as was shown, for example, in CREM-tau and Zmynd15 functions (Delmas et al. 1993; Yan et al. 2010).

In the present study, we used electroporation to transfect shRNA plasmids in the knockdown experiment. To achieve high transfection efficiency, neonatal testes were treated. Three HATs known to acetylate histone H3 at different lysine residues were selected specifically in the present study. Only knockdown of SRC-1 was associated with a significant under-expression of histone H3K9ac in round spermatids (by about 35%), with subsequent discernible induction of apoptosis of the transfected round spermatids. In fact, SRC-1 was relatively highly expressed in round spermatids compared with the other two HATs, GCN5 and ELP3 (Uhlen et al. 2010; Kapushesky et al. 2012), and SRC-1 regulated histone acetylation in specific residues including H3K9 (Spencer et al. 1997). During spermiogenesis, transcription generally ceases at about step 9 or 10 elongated spermatids (Soderstrom and Parvinen 1976), when the critical components of the transcription apparatus begin to dissociate from the chromatin (Zheng et al. 2008). It is possible that histone H3 hypoacetylation induced by SRC-1-knockdown triggered transcription termination in advance in the round spermatids, leading to their apoptosis.

Taken together, the present study clearly demonstrated that changes in histone H3 acetylation level resulted in round spermatid dysfunction, suggesting that the proper histone H3 acetylation is critical for the progression of spermiogenesis. At this stage, the correlation between histone H3

acetylation and special haploid gene transcription in round spermatids deserves further investigation.

Acknowledgments This study was supported in part by a Grant-in-Aid for Scientific Research from the Japan Society for the Promotion of Science (No. 18390060 to Koji, T.).

References

- Berger SL (2002) Histone modifications in transcriptional regulation. *Curr Opin Genet Dev* 12 (2):142-148. doi:10.1016/S0959-437X(02)00279-4
- Boivin AJ, Momparler LF, Hurtubise A, Momparler RL (2002) Antineoplastic action of 5-aza-2'-deoxycytidine and phenylbutyrate on human lung carcinoma cells. *Anticancer Drugs* 13 (8):869-874. doi:10.1097/00001813-200209000-00013
- Butler LM, Zhou X, Xu WS, Scher HI, Rifkind RA, Marks PA, Richon VM (2002) The histone deacetylase inhibitor SAHA arrests cancer cell growth, up-regulates thioredoxin-binding protein-2, and down-regulates thioredoxin. *Proc Natl Acad Sci U S A* 99 (18):11700-11705. doi:10.1073/pnas.182372299
- Calvaruso G, Carabillo M, Giuliano M, Lauricella M, D'Anneo A, Vento R, Tesoriere G (2001) Sodium phenylbutyrate induces apoptosis in human retinoblastoma Y79 cells: the effect of combined treatment with the topoisomerase I-inhibitor topotecan. *Int J Oncol* 18 (6):1233-1237. doi:10.3892/ijo.18.6.1233
- Cervoni N, Szyf M (2001) Demethylase activity is directed by histone acetylation. *J Biol Chem* 276 (44):40778-40787. doi:10.1074/jbc.M103921200
- Creasy DM, Ford GR, Gray TJ (1990) The morphogenesis of cyclohexylamine-induced testicular atrophy in the rat: in vivo and in vitro studies. *Exp Mol Pathol* 52 (2):155-169. doi:10.1016/0014-4800(90)90001-T
- Damavandi E, Hishikawa Y, Izumi S-i, Shin M, Koji T (2002) Involvement of Bax redistribution in the induction of germ cell apoptosis in neonatal mouse testes. *Acta Histochem Cytochem* 35 (6):449-459. doi:10.1679/aohc.66.1
- de Ruijter AJ, van Gennip AH, Caron HN, Kemp S, van Kuilenburg AB (2003) Histone deacetylases (HDACs): characterization of the classical HDAC family. *Biochem J* 370 (Pt 3):737-749. doi:10.1042/BJ20021321
- Delfino F, Walker WH (1998) Stage-specific nuclear expression of NF-kappaB in mammalian testis. *Mol Endocrinol* 12 (11):1696-1707. doi:10.1210/mend.12.11.0194
- Delmas V, van der Hoorn F, Mellstrom B, Jegou B, Sassone-Corsi P (1993) Induction of CREM activator proteins in spermatids: down-stream targets and implications for haploid germ cell differentiation. *Mol Endocrinol* 7 (11):1502-1514. doi:10.1210/mend.7.11.8114765
- Detich N, Bovenzi V, Szyf M (2003) Valproate induces replication-independent active DNA demethylation. *J Biol Chem* 278 (30):27586-27592. doi:10.1074/jbc.M303740200
- Feinman R, Clarke KO, Harrison LE (2002) Phenylbutyrate-induced apoptosis is associated with

- inactivation of NF-kappaB IN HT-29 colon cancer cells. *Cancer Chemother Pharmacol* 49 (1):27-34. doi:10.1007/s00280-001-0390-6
- Gavrieli Y, Sherman Y, Ben-Sasson SA (1992) Identification of programmed cell death in situ via specific labeling of nuclear DNA fragmentation. *J Cell Biol* 119 (3):493-501. doi:10.1083/jcb.119.3.493
- Giles RH, Peters DJ, Breuning MH (1998) Conjunction dysfunction: CBP/p300 in human disease. *Trends Genet* 14 (5):178-183. doi:10.1016/S0168-9525(98)01438-3
- Govin J, Lestrat C, Caron C, Pivot-Pajot C, Rousseaux S, Khochbin S (2006) Histone acetylation-mediated chromatin compaction during mouse spermatogenesis. *Ernst Schering Res Found Workshop* (57):155-172. doi:10.1007/3-540-37633-X_9
- Hazzouri M, Pivot-Pajot C, Faure AK, Usson Y, Pelletier R, Sele B, Khochbin S, Rousseaux S (2000) Regulated hyperacetylation of core histones during mouse spermatogenesis: involvement of histone deacetylases. *Eur J Cell Biol* 79 (12):950-960. doi:10.1078/0171-9335-00123
- Iannitti T, Palmieri B (2011) Clinical and experimental applications of sodium phenylbutyrate. *Drugs R D* 11 (3):227-249. doi:10.2165/11591280-000000000-00000
- Kapushesky M, Adamusiak T, Burdett T, Culhane A, Farne A, Filippov A, Holloway E, Klebanov A, Kryvych N, Kurbatova N, Kurnosov P, Malone J, Melnichuk O, Petryszak R, Pultsin N, Rustici G, Tikhonov A, Travillian R, Williams E, Zorin A, Parkinson H, Brazma A (2012) Gene Expression Atlas update--a value-added database of microarray and sequencing-based functional genomics experiments. *Nucleic Acids Res* 40:D1077-1081. doi:10.1093/nar/gkr913
- Koji T, Kondo S, Hishikawa Y, An S, Sato Y (2008) In situ detection of methylated DNA by histone endonuclease-linked detection of methylated DNA sites: a new principle of analysis of DNA methylation. *Histochem Cell Biol* 130 (5):917-925. doi:10.1007/s00418-008-0487-7
- Kondo Y, Shen L, Yan PS, Huang TH, Issa JP (2004) Chromatin immunoprecipitation microarrays for identification of genes silenced by histone H3 lysine 9 methylation. *Proc Natl Acad Sci U S A* 101 (19):7398-7403. doi:10.1073/pnas.0306641101
- Kopera IA, Bilinska B, Cheng CY, Mruk DD (2010) Sertoli-germ cell junctions in the testis: a review of recent data. *Philos Trans R Soc Lond B Biol Sci* 365 (1546):1593-1605. doi:10.1098/rstb.2009.0251
- Kuo MH, Allis CD (1998) Roles of histone acetyltransferases and deacetylases in gene regulation. *Bioessays* 20 (8):615-626. doi:10.1002/(SICI)1521-1878(199808)20:8<615::AID-BIES4>3.0.CO;2-H
- Lee B, Rhead W, Diaz GA, Scharschmidt BF, Mian A, Shchelochkov O, Marier JF, Beliveau M, Mauney J, Dickinson K, Martinez A, Gargosky S, Mokhtarani M, Berry SA (2010) Phase 2 comparison of a novel ammonia scavenging agent with sodium phenylbutyrate in patients with urea cycle disorders: safety, pharmacokinetics and ammonia control. *Mol Genet Metab* 100 (3):221-228. doi:10.1016/j.ymgme.2010.03.014
- Lin YN, Matzuk MM (2005) High-throughput discovery of germ-cell-specific genes. *Semin Reprod Med* 23 (3):201-212. doi:10.1055/s-2005-872448
- Louis M, Rosato RR, Brault L, Osbild S, Battaglia E, Yang XH, Grant S, Bagrel D (2004) The histone deacetylase inhibitor sodium butyrate induces breast cancer cell apoptosis through diverse cytotoxic actions including glutathione depletion and oxidative stress. *Int J Oncol* 25 (6):1701-1711. doi:10.3892/ijo.25.6.1701
- Meister G, Tuschl T (2004) Mechanisms of gene silencing by double-stranded RNA. *Nature* 431

- (7006):343-349. doi:10.1038/nature02873
- Milkevitch M, Shim H, Pilatus U, Pickup S, Wehrle JP, Samid D, Poptani H, Glickson JD, Delikatny EJ (2005) Increases in NMR-visible lipid and glycerophosphocholine during phenylbutyrate-induced apoptosis in human prostate cancer cells. *Biochim Biophys Acta* 1734 (1):1-12. doi:10.1016/j.bbaliip.2005.01.008
- Mizzen CA, Yang XJ, Kokubo T, Brownell JE, Bannister AJ, Owen-Hughes T, Workman J, Wang L, Berger SL, Kouzarides T, Nakatani Y, Allis CD (1996) The TAF(II)250 subunit of TFIID has histone acetyltransferase activity. *Cell* 87 (7):1261-1270. doi:10.1016/S0092-8674(00)81821-8
- Munshi A, Shafi G, Aliya N, Jyothy A (2009) Histone modifications dictate specific biological readouts. *J Genet Genomics* 36 (2):75-88. doi:10.1016/S1673-8527(08)60094-6
- Nair M, Nagamori I, Sun P, Mishra DP, Rheume C, Li B, Sassone-Corsi P, Dai X (2008) Nuclear regulator Pygo2 controls spermiogenesis and histone H3 acetylation. *Dev Biol* 320 (2):446-455. doi:10.1016/j.ydbio.2008.05.553
- Natsume-Kitatani Y, Shiga M, Mamitsuka H (2011) Genome-wide integration on transcription factors, histone acetylation and gene expression reveals genes co-regulated by histone modification patterns. *PLoS One* 6 (7):e22281. doi:10.1371/journal.pone.0022281
- Neal KC, Pannuti A, Smith ER, Lucchesi JC (2000) A new human member of the MYST family of histone acetyl transferases with high sequence similarity to *Drosophila* MOF. *Biochim Biophys Acta* 1490 (1-2):170-174. doi:10.1016/S0167-4781(99)00211-0
- Neuwald AF, Landsman D (1997) GCN5-related histone N-acetyltransferases belong to a diverse superfamily that includes the yeast SPT10 protein. *Trends Biochem Sci* 22 (5):154-155. doi:10.1016/S0968-0004(97)01034-7
- Penttila TL, Yuan L, Mali P, Hoog C, Parvinen M (1995) Haploid gene expression: temporal onset and storage patterns of 13 novel transcripts during rat and mouse spermiogenesis. *Biol Reprod* 53 (3):499-510. doi:10.1095/biolreprod53.3.499
- Petri S, Kiaei M, Kipiani K, Chen J, Calingasan NY, Crow JP, Beal MF (2006) Additive neuroprotective effects of a histone deacetylase inhibitor and a catalytic antioxidant in a transgenic mouse model of amyotrophic lateral sclerosis. *Neurobiol Dis* 22 (1):40-49. doi:10.1016/j.nbd.2005.09.013
- Roosen-Runge EC (1962) The process of spermatogenesis in mammals. *Biol Rev Camb Philos Soc* 37:343-377. doi:10.1111/j.1469-185X.1962.tb01616.x
- Roy A, Ghosh A, Jana A, Liu X, Brahmachari S, Gendelman HE, Pahan K (2012) Sodium phenylbutyrate controls neuroinflammatory and antioxidant activities and protects dopaminergic neurons in mouse models of Parkinson's disease. *PLoS One* 7 (6):e38113. doi:10.1371/journal.pone.0038113
- Ruefli AA, Ausserlechner MJ, Bernhard D, Sutton VR, Tainton KM, Kofler R, Smyth MJ, Johnstone RW (2001) The histone deacetylase inhibitor and chemotherapeutic agent suberoylanilide hydroxamic acid (SAHA) induces a cell-death pathway characterized by cleavage of Bid and production of reactive oxygen species. *Proc Natl Acad Sci U S A* 98 (19):10833-10838. doi:10.1073/pnas.191208598
- Saito M, Kumamoto K, Robles AI, Horikawa I, Furusato B, Okamura S, Goto A, Yamashita T, Nagashima M, Lee TL, Baxendale VJ, Rennert OM, Takenoshita S, Yokota J, Sesterhenn IA, Trivers GE, Hussain SP, Harris CC (2010) Targeted disruption of *Ing2* results in defective

- spermatogenesis and development of soft-tissue sarcomas. *PLoS One* 5 (11):e15541. doi:10.1371/journal.pone.0015541
- Shah P, Gau Y, Sabnis G (2014) Histone deacetylase inhibitor entinostat reverses epithelial to mesenchymal transition of breast cancer cells by reversing the repression of E-cadherin. *Breast Cancer Res Treat* 143 (1):99-111. doi:10.1007/s10549-013-2784-7
- Soderstrom KO, Parvinen M (1976) RNA synthesis in different stages of rat seminiferous epithelial cycle. *Mol Cell Endocrinol* 5 (3-4):181-199. doi:10.1016/0303-7207(76)90082-4
- Song N, Liu J, An S, Nishino T, Hishikawa Y, Koji T (2011) Immunohistochemical analysis of histone H3 modifications in germ cells during mouse spermatogenesis. *Acta Histochem Cytochem* 44 (4):183-190. doi:10.1267/ahc.11027
- Spencer TE, Jenster G, Burcin MM, Allis CD, Zhou J, Mizzen CA, McKenna NJ, Onate SA, Tsai SY, Tsai MJ, O'Malley BW (1997) Steroid receptor coactivator-1 is a histone acetyltransferase. *Nature* 389 (6647):194-198. doi:10.1038/38304
- Suka N, Suka Y, Carmen AA, Wu J, Grunstein M (2001) Highly specific antibodies determine histone acetylation site usage in yeast heterochromatin and euchromatin. *Mol Cell* 8 (2):473-479. doi:10.1016/S1097-2765(01)00301-X
- Uhlen M, Oksvold P, Fagerberg L, Lundberg E, Jonasson K, Forsberg M, Zwahlen M, Kampf C, Wester K, Hober S, Wernerus H, Björling L, Ponten F (2010) Towards a knowledge-based Human Protein Atlas. *Nat Biotechnol* 28 (12):1248-1250. doi:10.1038/nbt1210-1248
- Ungerstedt JS, Sowa Y, Xu WS, Shao Y, Dokmanovic M, Perez G, Ngo L, Holmgren A, Jiang X, Marks PA (2005) Role of thioredoxin in the response of normal and transformed cells to histone deacetylase inhibitors. *Proc Natl Acad Sci U S A* 102 (3):673-678. doi:10.1073/pnas.0408732102
- Vempati RK, Jayani RS, Notani D, Sengupta A, Galande S, Haldar D (2010) p300-mediated acetylation of histone H3 lysine 56 functions in DNA damage response in mammals. *J Biol Chem* 285 (37):28553-28564. doi:10.1074/jbc.M110.149393
- Wang RA, Nakane PK, Koji T (1998) Autonomous cell death of mouse male germ cells during fetal and postnatal period. *Biol Reprod* 58 (5):1250-1256. doi:10.1095/biolreprod58.5.1250
- Wittschieben BO, Otero G, de Bizemont T, Fellows J, Erdjument-Bromage H, Ohba R, Li Y, Allis CD, Tempst P, Svejstrup JQ (1999) A novel histone acetyltransferase is an integral subunit of elongating RNA polymerase II holoenzyme. *Mol Cell* 4 (1):123-128. doi:10.1016/S1097-2765(00)80194-X
- Yan W, Si Y, Slaymaker S, Li J, Zheng H, Young DL, Aslanian A, Saunders L, Verdin E, Charo IF (2010) Zmynd15 encodes a histone deacetylase-dependent transcriptional repressor essential for spermiogenesis and male fertility. *J Biol Chem* 285 (41):31418-31426. doi:10.1074/jbc.M110.116418
- Yomogida K, Yagura Y, Nishimune Y (2002) Electroporated transgene-rescued spermatogenesis in infertile mutant mice with a sertoli cell defect. *Biol Reprod* 67 (3):712-717. doi:10.1095/biolreprod.101.001743
- Yu KH, Weng LJ, Fu S, Piantadosi S, Gore SD (1999) Augmentation of phenylbutyrate-induced differentiation of myeloid leukemia cells using all-trans retinoic acid. *Leukemia* 13 (8):1258-1265. doi:10.1038/sj.leu.2401468
- Zhang Y, Kwon S, Yamaguchi T, Cubizolles F, Rousseaux S, Kneissel M, Cao C, Li N, Cheng HL, Chua K, Lombard D, Mizeracki A, Matthias G, Alt FW, Khochbin S, Matthias P (2008) Mice

lacking histone deacetylase 6 have hyperacetylated tubulin but are viable and develop normally. *Mol Cell Biol* 28 (5):1688-1701. doi:10.1128/MCB.01154-06

Zhang Z, Liu J, Kaur M, Krantz ID (2012) Characterization of DNA methylation and its association with other biological systems in lymphoblastoid cell lines. *Genomics* 99 (4):209-219. doi:10.1016/j.ygeno.2012.01.002

Zheng J, Xia X, Ding H, Yan A, Hu S, Gong X, Zong S, Zhang Y, Sheng HZ (2008) Erasure of the paternal transcription program during spermiogenesis: the first step in the reprogramming of sperm chromatin for zygotic development. *Dev Dyn* 237 (5):1463-1476. doi:10.1002/dvdy.21499

Zhou Q, Agoston AT, Atadja P, Nelson WG, Davidson NE (2008) Inhibition of histone deacetylases promotes ubiquitin-dependent proteasomal degradation of DNA methyltransferase 1 in human breast cancer cells. *Mol Cancer Res* 6 (5):873-883. doi:10.1158/1541-7786.MCR-07-0330

Figure captions

Fig. 1 Histological examination of paraffin-embedded sections of adult PBS- (**a-d**) and NaPB- (**e-h**) treated mouse testes at 6 h after treatment. H&E of seminiferous tubules at stage XII-I (**a, e**), IV-V (**b, f**), VIII (**c, g**) and X (**d, h**) are shown. The insets (**e'**) in **e** and (**f'**) in **f** are enlarged. Scale bars 20 μm (**e'**, **f'**) and 50 μm (**a-h**).

Fig. 2 Immunohistochemical detection of histone H3K9ac, H3K18ac and H3K23ac in paraffin-embedded sections of adult PBS- (**a-e**) and NaPB- (**f-j**) treated mouse testes at 6 h after treatment. Serial sections were used for H&E staining (**a, f**), immunohistochemical staining for H3K9ac (**b, g**), H3K18ac (**c, h**), and H3K23ac (**d, i**). As a negative control, PBS- (**e**) and NaPB- (**j**) treated sections of testes were reacted with normal rabbit IgG instead of specific antibodies. Seminiferous tubules at stage IV-V are shown. *Arrows*: abnormal round spermatid aggregates in NaPB-treated testes. Scale bars 50 μm .

Fig. 3 Effects of NaPB on testes weight and germ cell apoptosis in adult mouse. **a** Quantitative analysis of testes weight after NaPB treatment at various time points. Data are mean±SD. *P<0.05, **P<0.01. **b** Quantitative analysis of TUNEL-positive cells in PBS- and NaPB-treated testes at various time-points. Data are mean±SD. *P<0.05, **P<0.01. H&E staining of PBS- (**c**) and NaPB- (**e**) treated testes. TUNEL staining of PBS (**d**)- and NaPB (**f**)-treated testes at 6 h after treatment. *Arrowheads*: TUNEL-positive round spermatids. Scale bars 50 µm.

Fig. 4 Electron micrographs of round spermatids of PBS- and NaPB-treated adult mouse testes at 6 h after treatment. **a** Normal round spermatids in the PBS-treated testes. **b** Multinuclear syncytium consisting of round spermatids in NaPB-treated testes. *Asterisk*: fused area. Scale bars 2 µm.

Fig. 5 Immunohistochemical detection of Bax and Bcl-2 in adult PBS (**a, c, f**)- and NaPB (**b, d, g**)-treated mouse testes at 6 h after treatment. Serial sections were used for H&E staining (**a, b**), immunohistochemical staining for Bax (**c, d**) and Bcl-2 (**f, g**). The inserts (**d'**) in **d** and (**g'**) in **g** are enlarged. As a negative control, sections of NaPB (**e, h**)-treated testes were reacted with normal rabbit IgG instead of the specific antibodies. Scale bars 20 µm (**d', g'**) and 50 µm (**a-h**).

Fig. 6 Localization and quantitative analysis of non-methylated and methylated CCGG sequences by HELMET in paraffin-embedded sections of adult PBS (**a-d**)- and NaPB (**e-h**)-treated mouse testes at 6 h after treatment. **a, e** Staining for non-methylated CCGG sites by *HpaII* digestion. **b, f** Staining for methylated CCGG sites by *MspI* digestion. Merged images are shown in (**c, g**). DAPI staining is shown in (**d, h**). **i** Quantitative analysis of global CCGG methylation in the round spermatid aggregates of

adult NaPB-treated mouse testes at 6 h after treatment measured by HELMET. Global CCGG methylation represents the ratio of methylated CCGG/non-methylated CCGG, which was normalized to that of round spermatids in PBS-treated testes. Data are mean \pm SD. **P<0.01. The inserts (**c'**, **g'**) are round spermatids (**c'**) in PBS (**c**)-treated testes and abnormal round spermatid aggregates (**g'**) in NaPB (**g**)-treated testes. Scale bars 50 μ m.

Fig. 7 Immunohistochemical detection of 5mC, 5hmC and Dnmt1 in NaPB-treated testes. Paraffin embedded sections from adult PBS (**a-d**)- and NaPB (**f-i**)-treated mouse testes at 6h after treatment were reacted with anti-5mC (**b, g**), anti-5hmC (**c, h**) and anti-Dnmt1 (**d, i**) antibodies. The inserts (**b'**, **c'**, **d'**, **g'**, **h'**, **i'**) are enlarged. *Arrowheads* round spermatids with reduced 5mC staining; *arrows* 5hmC-positive round spermatids; *open arrows* round spermatids with reduced Dnmt1 staining. As a negative control, sections of NaPB (**e, j**)-treated testes were reacted with normal rabbit IgG (**e**) and mouse IgG (**j**) instead of the specific antibodies. Scale bars 50 μ m.

Fig. 8 Double staining for TUNEL (**a**) and non-methylated CCGG sequences (**b**) by HELMET with *HpaII* digestion in paraffin-embedded sections of adult NaPB-treated mouse testes at 6 h after treatment. The merged image is shown in (**c**). DAPI staining appears in (**d**). *Arrows* TUNEL-positive round spermatids with elevated non-methylated CCGG level; *arrowheads* TUNEL-negative round spermatids with elevated non-methylated CCGG level. Scale bars 50 μ m.

Fig. 9 Stereomicroscopic views and immunohistochemical analysis of shRNA plasmid transfected 28-day-old neonatal mouse testes at day 10 post transfection. **a** GFP expression in the testes after

transfection. Double immunofluorescence staining of GFP (**b, e**) and SRC-1 (**c, f**) in LacZ (**b-d**)- and SRC-1 (**e-g**)-shRNA plasmids transfected testes. DAPI staining is shown in (**d, g**). *Arrows* GFP-positive round spermatid in LacZ-shRNA transfected testes; *arrowheads* GFP-positive round spermatid in SRC-1-shRNA transfected testes. Inserts (**c'**) in **c** and (**f'**) in **f** are enlarged. Scale bars 10 μm .

Fig. 10 Double immunofluorescence staining and quantitative analysis of GFP and H3K9ac in shRNA plasmid transfected 28-day-old neonatal mouse testes at day 10 post transfection. Double immunofluorescence staining of GFP (**a, c**) and H3K9ac (**b, d**) in LacZ (**a, b**)- and SRC-1 (**c, d**)-shRNA transfected testes. *Arrows* GFP-positive round spermatids in LacZ-shRNA transfected testes; *arrowheads* GFP-positive round spermatids in SRC-1-shRNA transfected testes. Inserts (**b'**) in **b** and (**d'**) in **d** are enlarged. Scale bars 50 μm . **e** Quantitative analysis of H3K9ac signal in GFP-positive round spermatids of LacZ- and SRC-1-shRNA transfected testes. Fluorescence intensity of H3K9ac, which normalized to that of round spermatids in LacZ-shRNA transfected testes is presented as mean \pm SD. *P<0.05.

Fig. 11 TUNEL staining and quantitative analysis of LacZ- and SRC-1-shRNA transfected 28-day-old neonatal mouse testes at day 10 post transfection. H&E staining of paraffin sections of LacZ (**a**)- and SRC-1 (**c**)-shRNA transfected testes. TUNEL staining of apoptotic germ cells in LacZ (**b**)- and SRC-1 (**d**)-shRNA transfected testes. *Arrowheads* TUNEL-positive round spermatids. Scale bars 50 μm . **E** Quantitative analysis of TUNEL-positive round spermatids in LacZ- and SRC-1-shRNA transfected testes. Data are mean \pm SD. *P<0.05.

Fig. S1 TUNEL staining and immunohistochemical detection of 8-OHdG in adult NaPB (**a-d**)-treated mouse testes at 6 h after treatment and SAHA (**e-h**)-treated mouse testes at 12 h after treatment. Serial sections were used for H&E staining (**a, e**), TUNEL staining (**b, f**), immunohistochemical staining for 8-OHdG (**c, g**). *Arrowheads* TUNEL-positive cells without 8-OHdG signals; *arrows* TUNEL-positive cells with 8-OHdG signals. The inserts (**b'**) in **b** and (**c'**) in **c** are enlarged. As a negative control, sections of NaPB (**d**)- and SAHA (**h**)-treated testes were reacted with normal mouse IgG instead of the specific antibody. Scale bars 50 μ m.

Fig. S2 Immunohistochemical detection of histone H3K9ac, H3K18ac and H3K23ac in paraffin-embedded sections of adult DMSO- (**a-e**) and SAHA- (**f-j**) treated mouse testes at 12 h after treatment. Serial sections were used for H&E staining (**a, f**), immunohistochemical staining for H3K9ac (**b, g**), H3K18ac (**c, h**), and H3K23ac (**d, i**). As a negative control, DMSO- (**e**) and SAHA- (**j**) treated sections of testes were reacted with normal rabbit IgG instead of specific antibodies. Seminiferous tubules at stage VI-VII are shown. Scale bars 50 μ m.

Fig. S3 Immunofluorescence detection of GFP in LacZ- (**a-c**), SRC-1- (**d-f**) shRNA transfected and non-transfected (**g-i**) 28-day-old neonatal mouse testes. **a, d, g** immunofluorescence staining of GFP. **b, e, h** As a negative control, sections were reacted with normal mouse IgG instead of the specific antibody. **c, f, i** DAPI staining. *Arrowheads* GFP-positive cells; *asterisks* nonspecific fluorescence signals from the secondary antibody in interstitial Leydig cells. Scale bars 50 μ m.

Fig. S4 Double immunofluorescence staining of GFP and GCN5 in LacZ- and GCN5-shRNA plasmid transfected 28-day-old neonatal mouse testes at day 10 post transfection. **a-f** Double immunofluorescence staining of GFP (**a, d**) and GCN5 (**b, e**) in LacZ- (**a-c**) and GCN5- (**d-f**) shRNA transfected testes. *Arrows* GFP-positive round spermatids in LacZ-shRNA transfected testes; *arrowheads* GFP-positive round spermatids in GCN5-shRNA transfected testes. Scale bars 10 μm .

Fig. S5 Double immunofluorescence staining of GFP and ELP3 in LacZ- and ELP3-shRNA plasmid transfected 28-day-old neonatal mouse testes at day 10 post transfection. **a-f** Double immunofluorescence staining of GFP (**a, d**) and ELP3 (**b, e**) in LacZ- (**a-c**) and ELP3- (**d-f**) shRNA transfected testes. *Arrows* GFP-positive round spermatids in LacZ-shRNA transfected testes; *arrowheads* GFP-positive round spermatids in ELP3-shRNA transfected testes. Scale bars 10 μm .

Fig. S6 Double immunofluorescence staining of GFP and H3K9ac; GFP and H3K18ac; GFP and H3K23ac in shRNA plasmid transfected 28-day-old neonatal mouse testes at day 10 post transfection. **a-d** Double immunofluorescence staining of GFP and H3K9ac in LacZ- (**a**), SRC-1- (**b**), GCN5- (**c**) and ELP3- (**d**) shRNA transfected testes. **e-h** Double immunofluorescence staining of GFP and H3K18ac in LacZ- (**e**), SRC-1- (**f**), GCN5- (**g**) and ELP3- (**h**) shRNA transfected testes. **i-l** Double immunofluorescence staining of GFP and H3K23ac in LacZ- (**i**), SRC-1- (**j**), GCN5- (**k**) and ELP3- (**l**) shRNA transfected testes. *Arrowheads* GFP-positive round spermatid in SRC-1-shRNA transfected testes with reduced H3K9ac staining. Scale bar 20 μm .

Fig. S7 Methylation level of CCGG sites in adjacent section of NaPB-treated testis at 6 h after

treatment by HELMET method using DAB staining. Adjacent sections of paraffin-embedded mouse testes were used for H&E staining, TUNEL, non-methylated CCGG sites and methylated CCGG sites.

a H&E staining. **b** TUNEL staining. **c** Blockade of 3'-OH ends with dideoxynucleotides by TdT.

After blockade, the section was labeled with biotin-16-dUTP by TdT and the incorporated biotin was detected with HRP-anti-biotin. No signals were observed. **d** Staining for non-methylated CCGG sites.

After the blockade procedure described in **c**, the section was digested with *HpaII*, labeled with biotin-16-dUTP and visualized by enzyme-immunohistochemistry with HRP-anti-biotin. **e** Blockade of *HpaII* cutting sites with dideoxynucleotides by TdT. The section was digested with *HpaII* and the cutting sites were blocked with a dideoxynucleotide mixture. Then the section was processed in a manner similar to that described in **c**. **f** Staining for methylated CCGG sites. After blockade of *HpaII* cutting sites with dideoxynucleotides, the section was digested with *MspI* and the cutting sites were labeled with biotin-16-dUTP and visualized with HRP-anti-biotin. *Arrows* TUNEL-positive round spermatids with elevated non-methylated CCGG sites; *arrowheads* TUNEL-negative round spermatids with elevated non-methylated CCGG sites. Scale bars 50 μm .

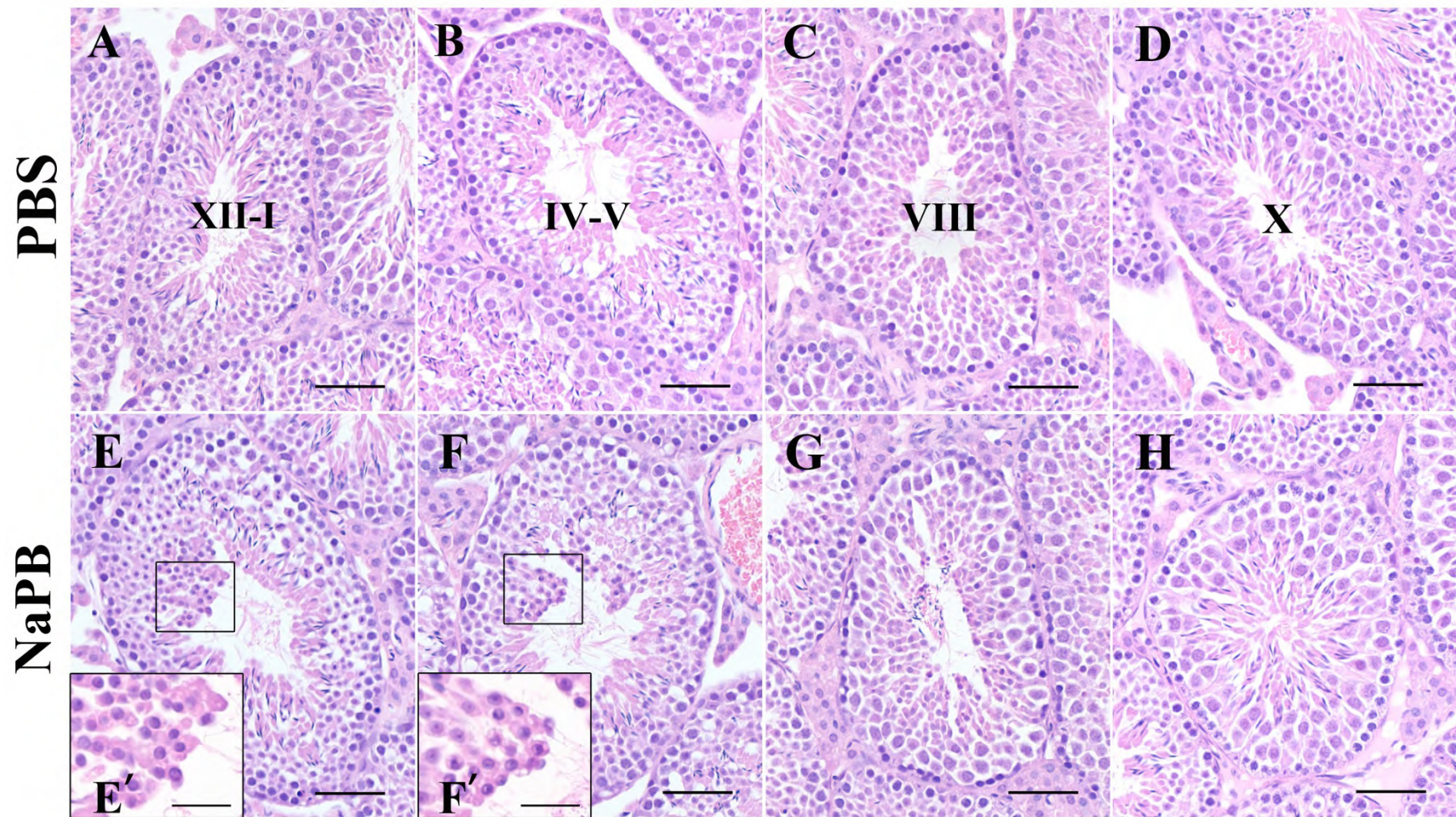


Fig. 1

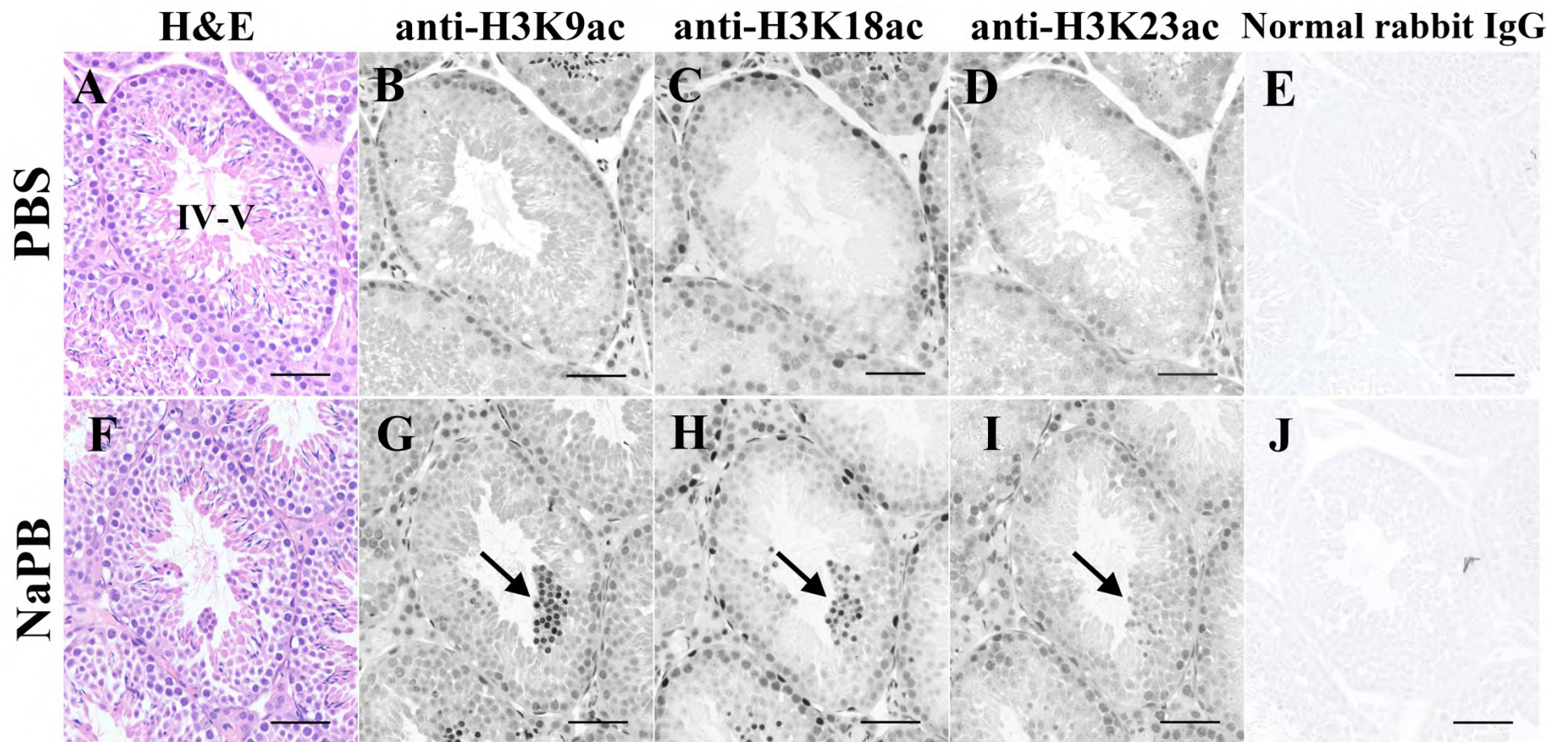


Fig. 2

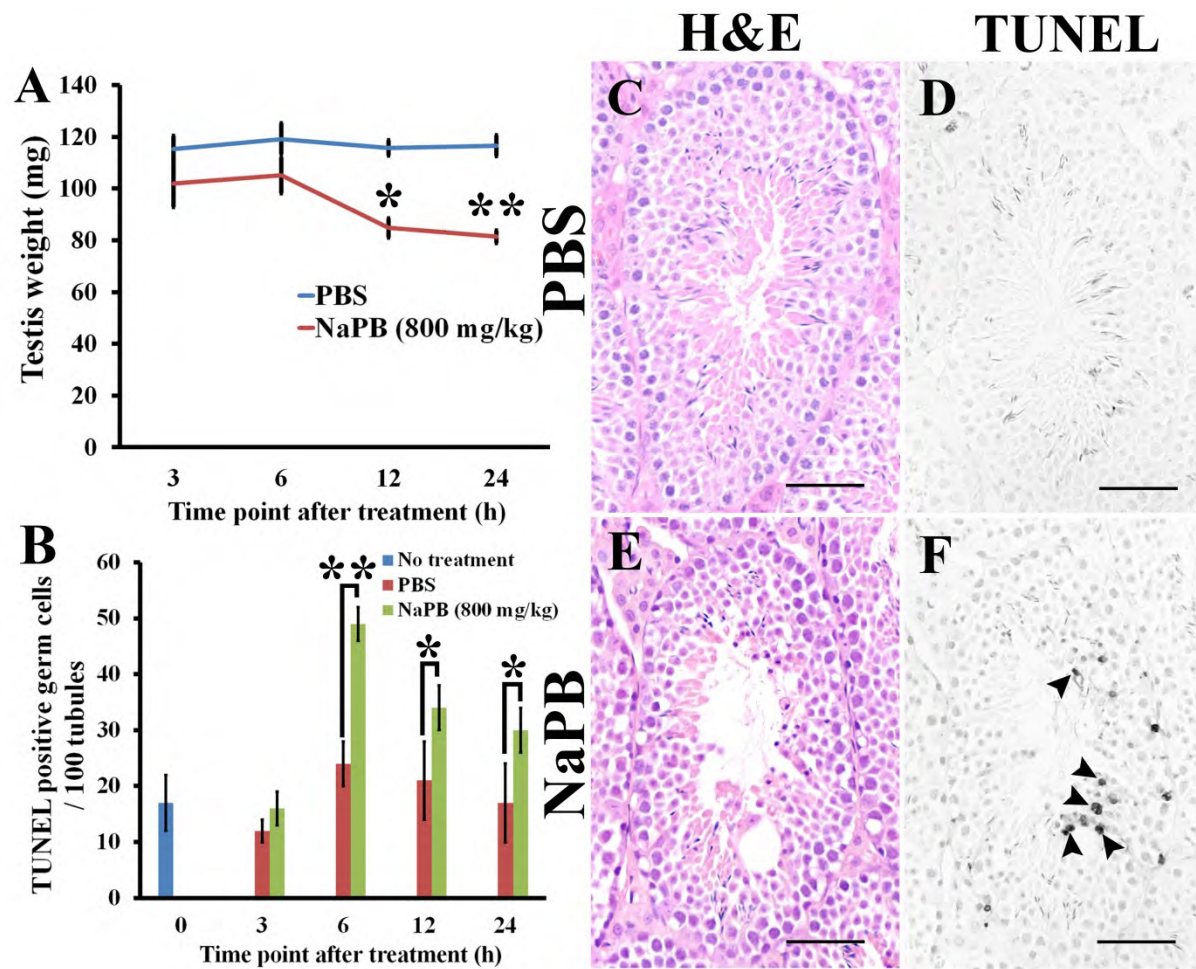


Fig. 3

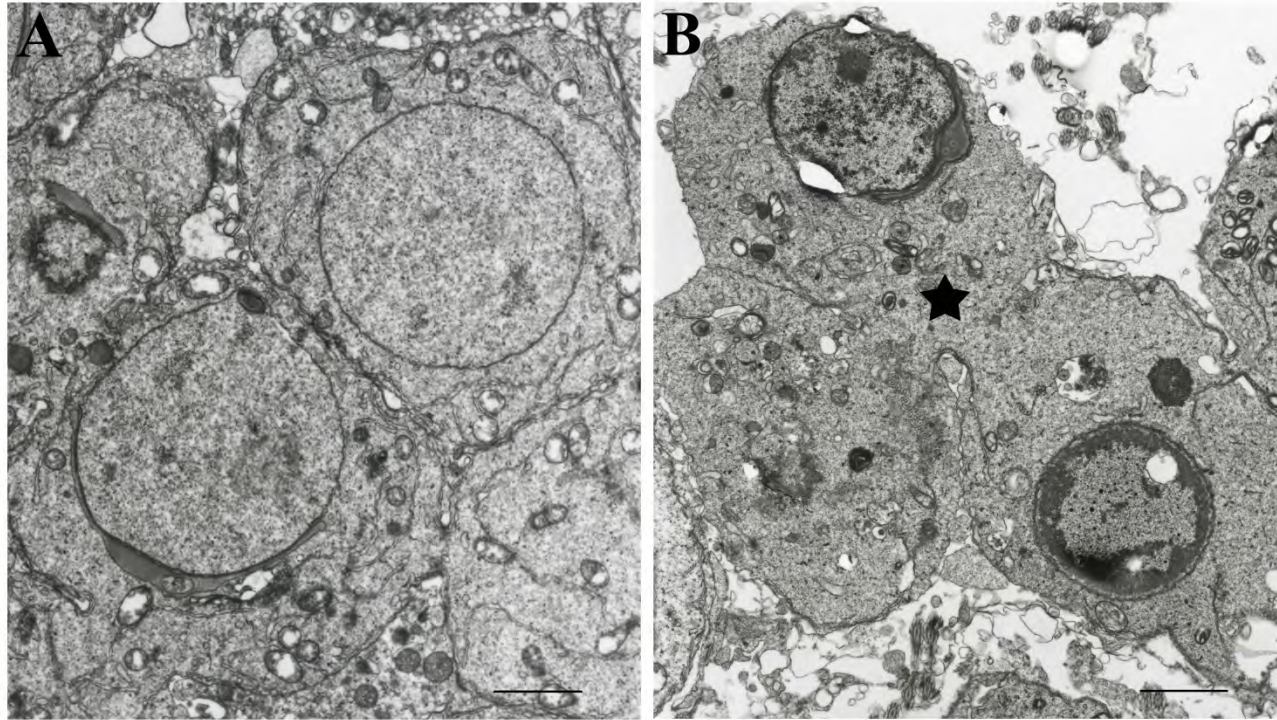


Fig. 4

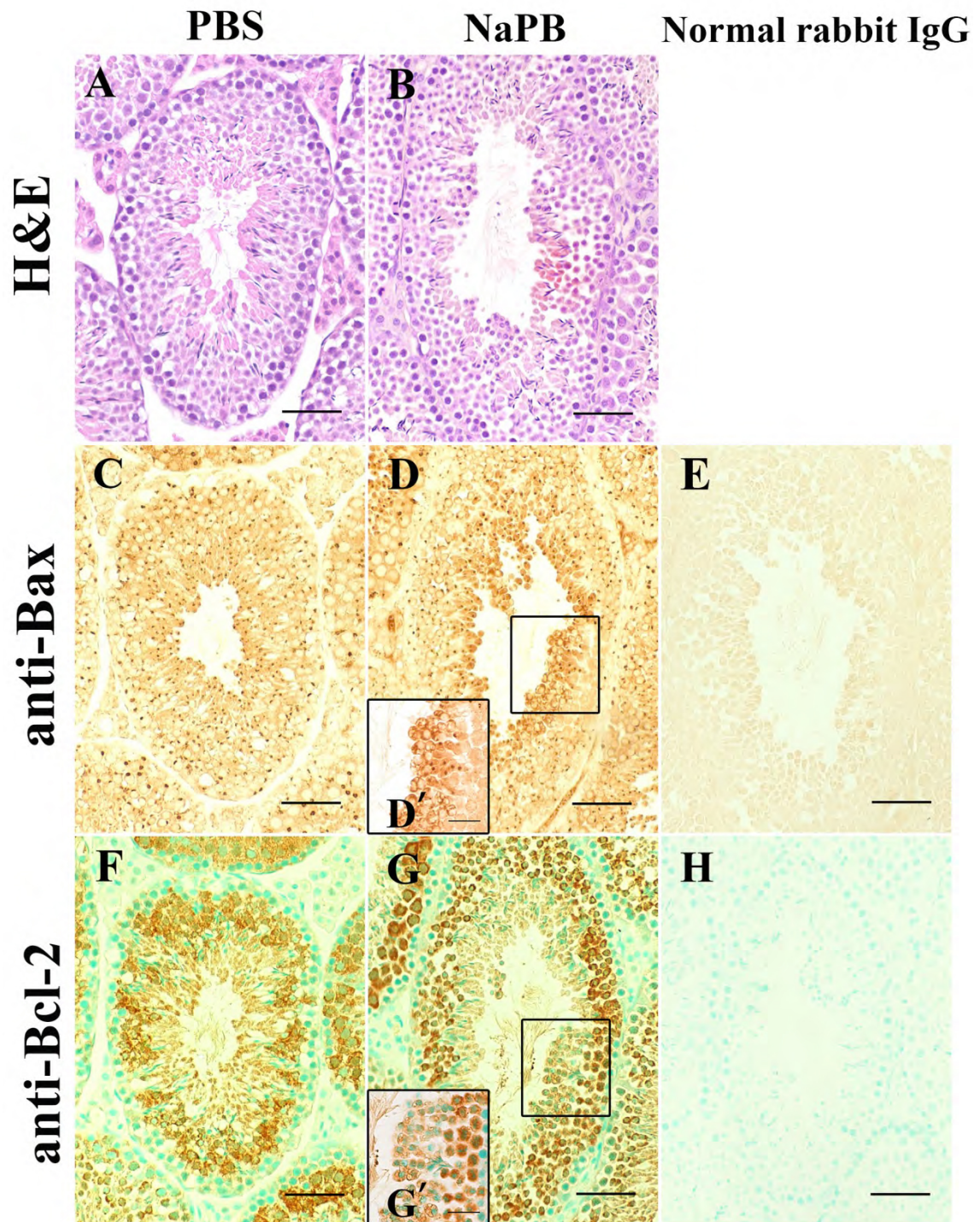


Fig. 5

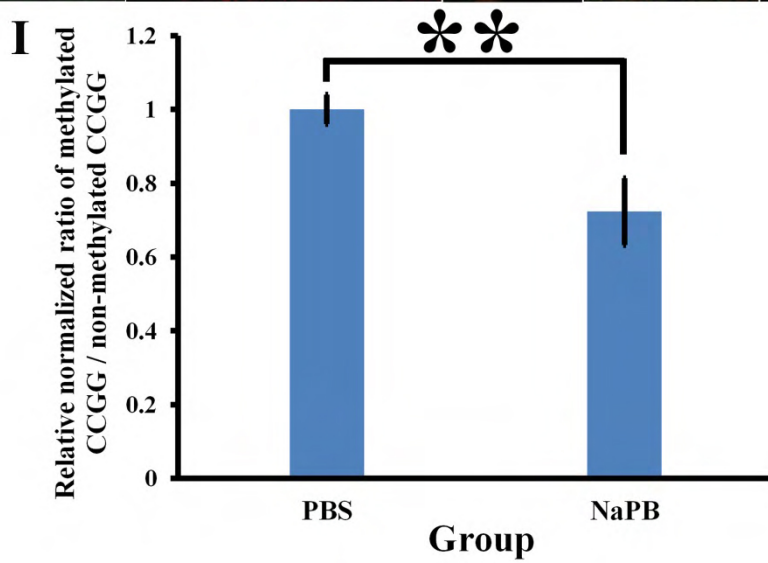
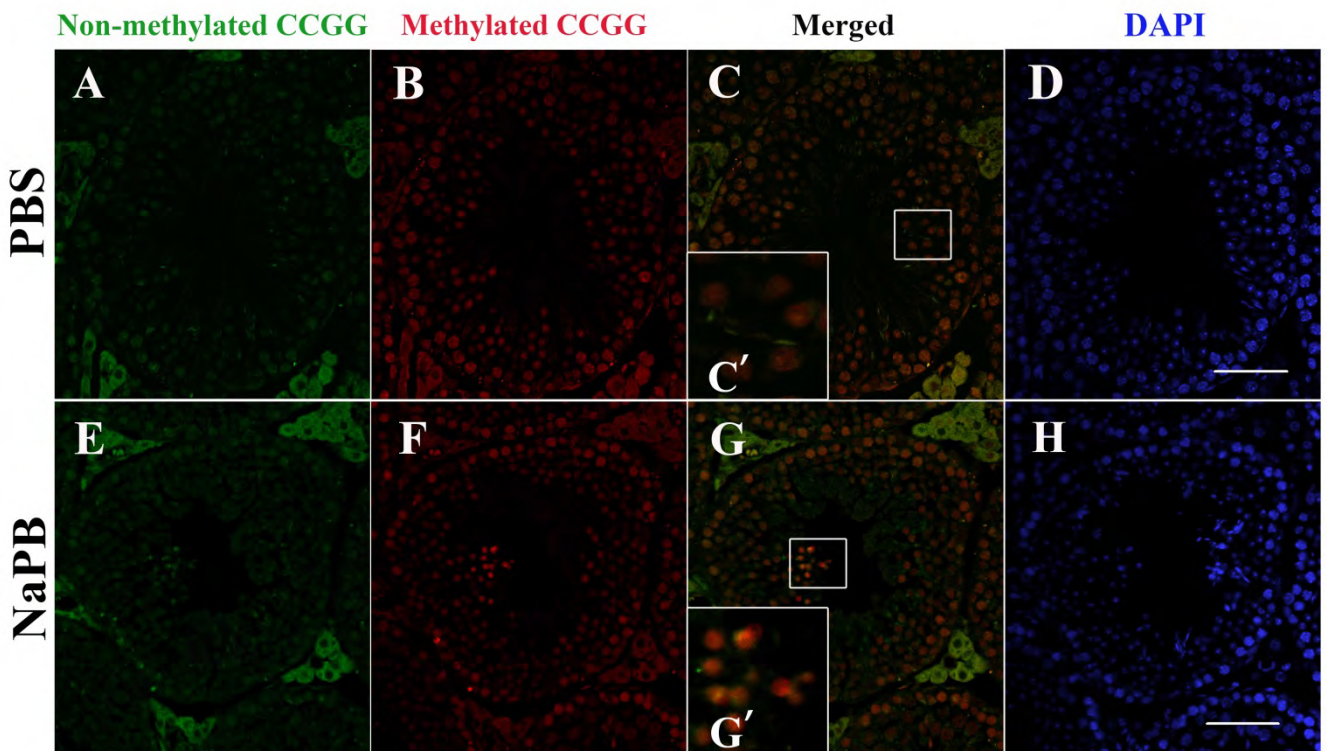


Fig. 6

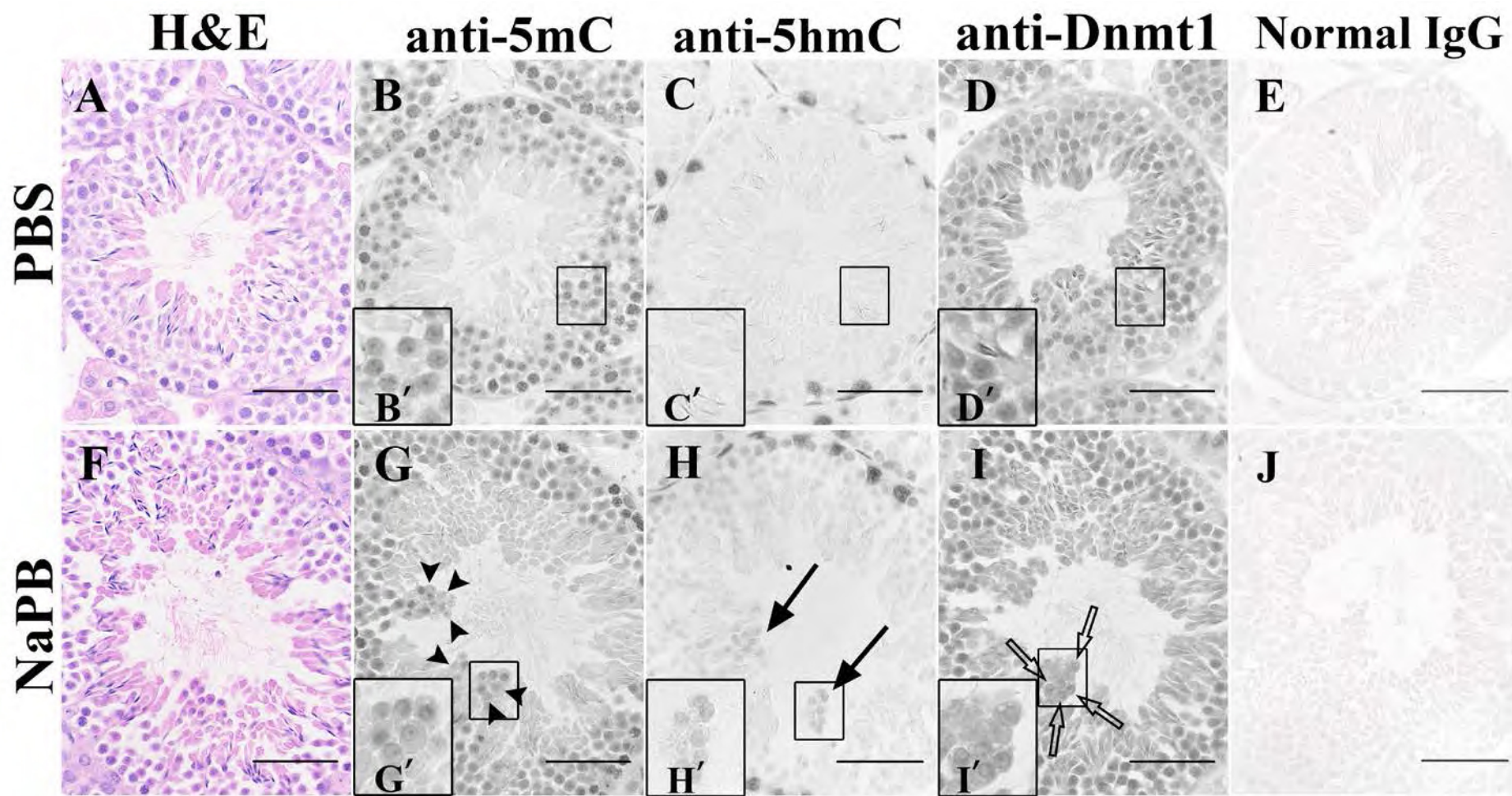


Fig. 7

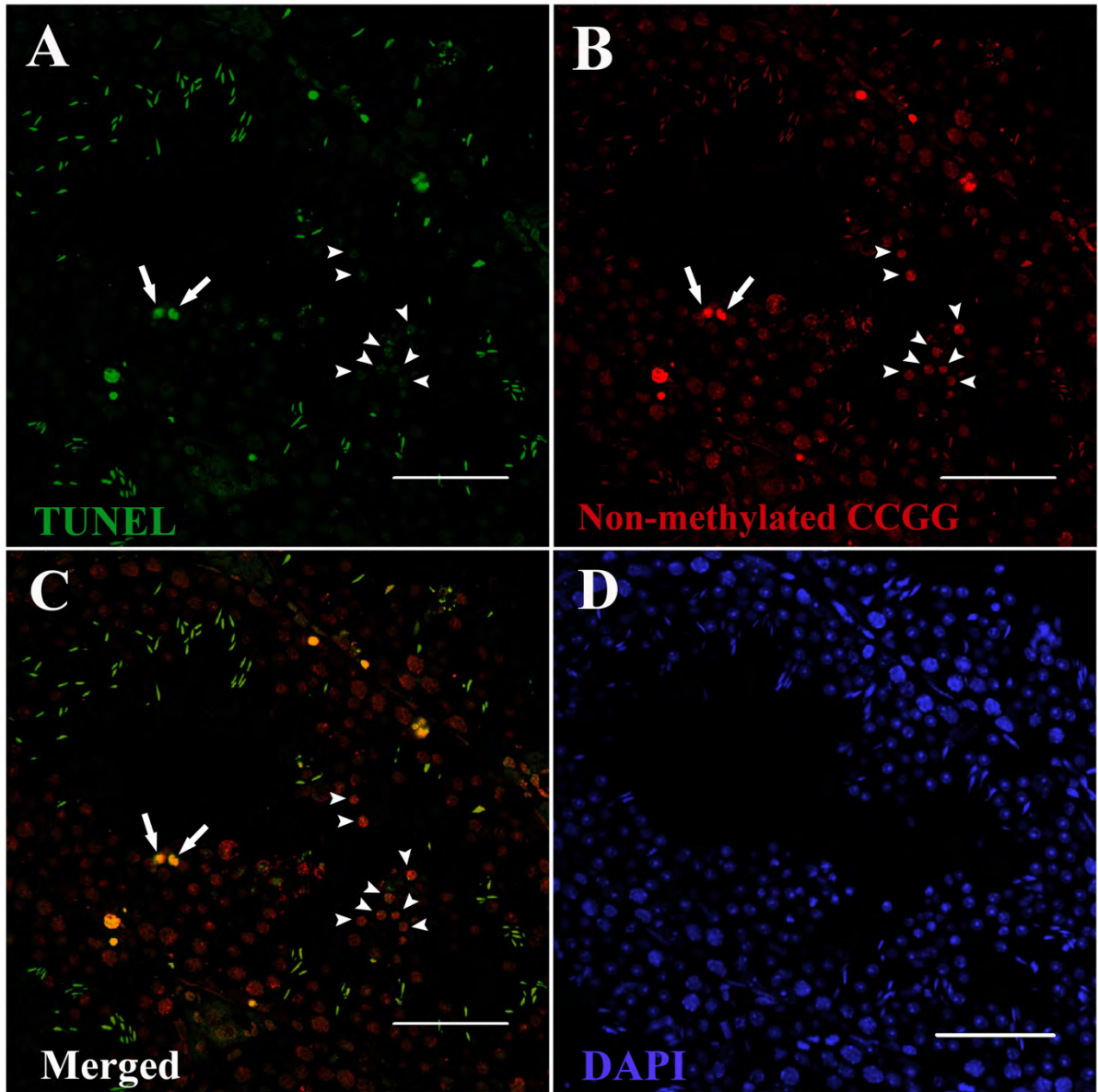


Fig. 8

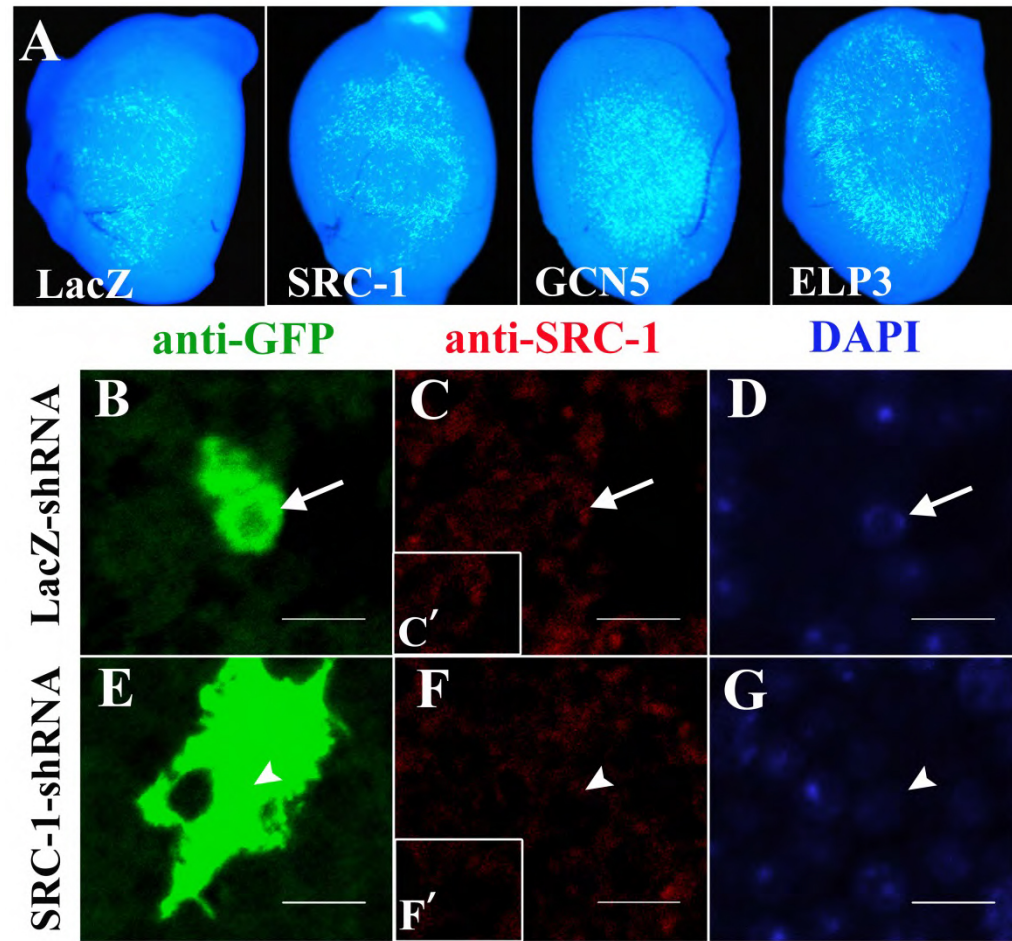


Fig. 9

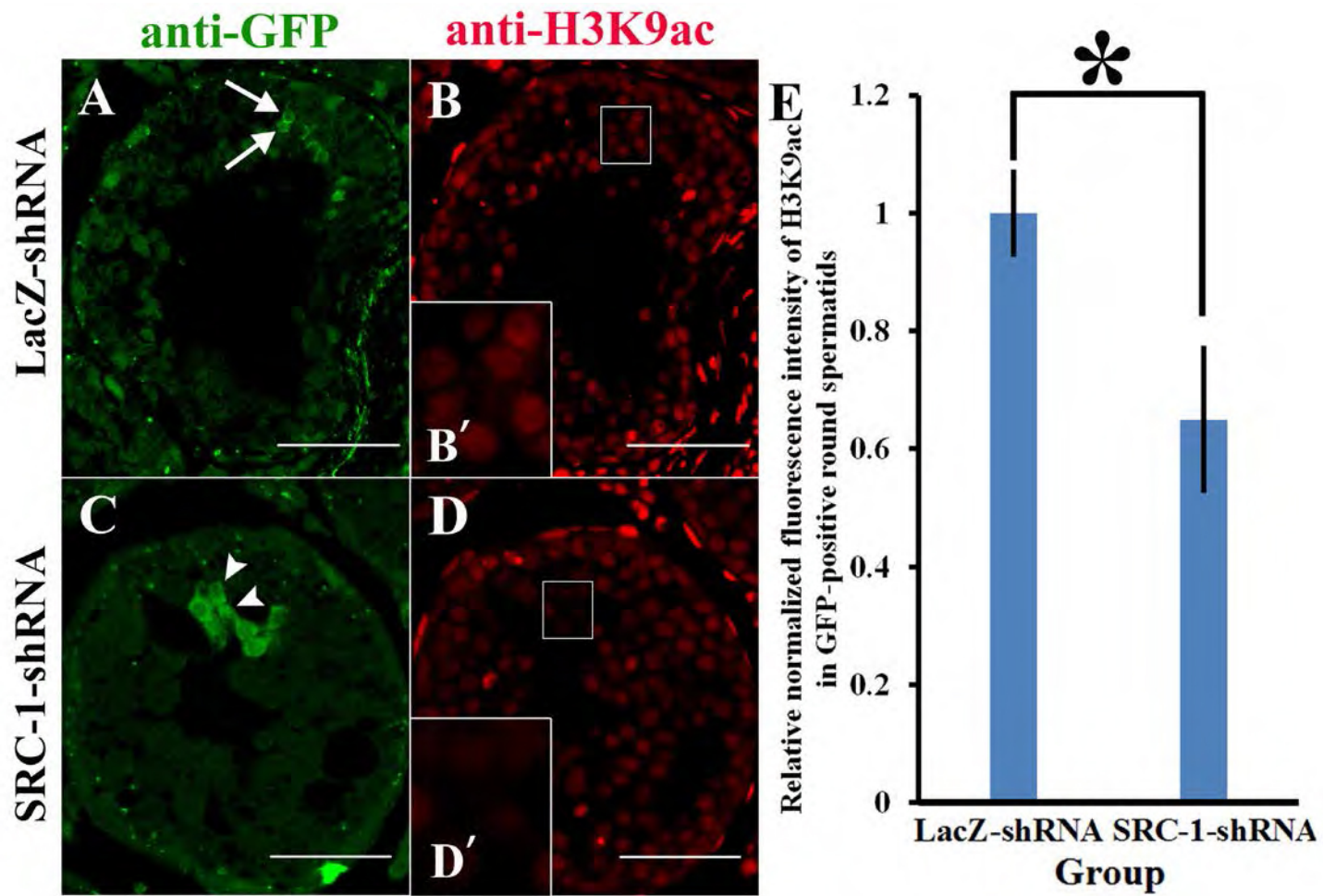


Fig. 10

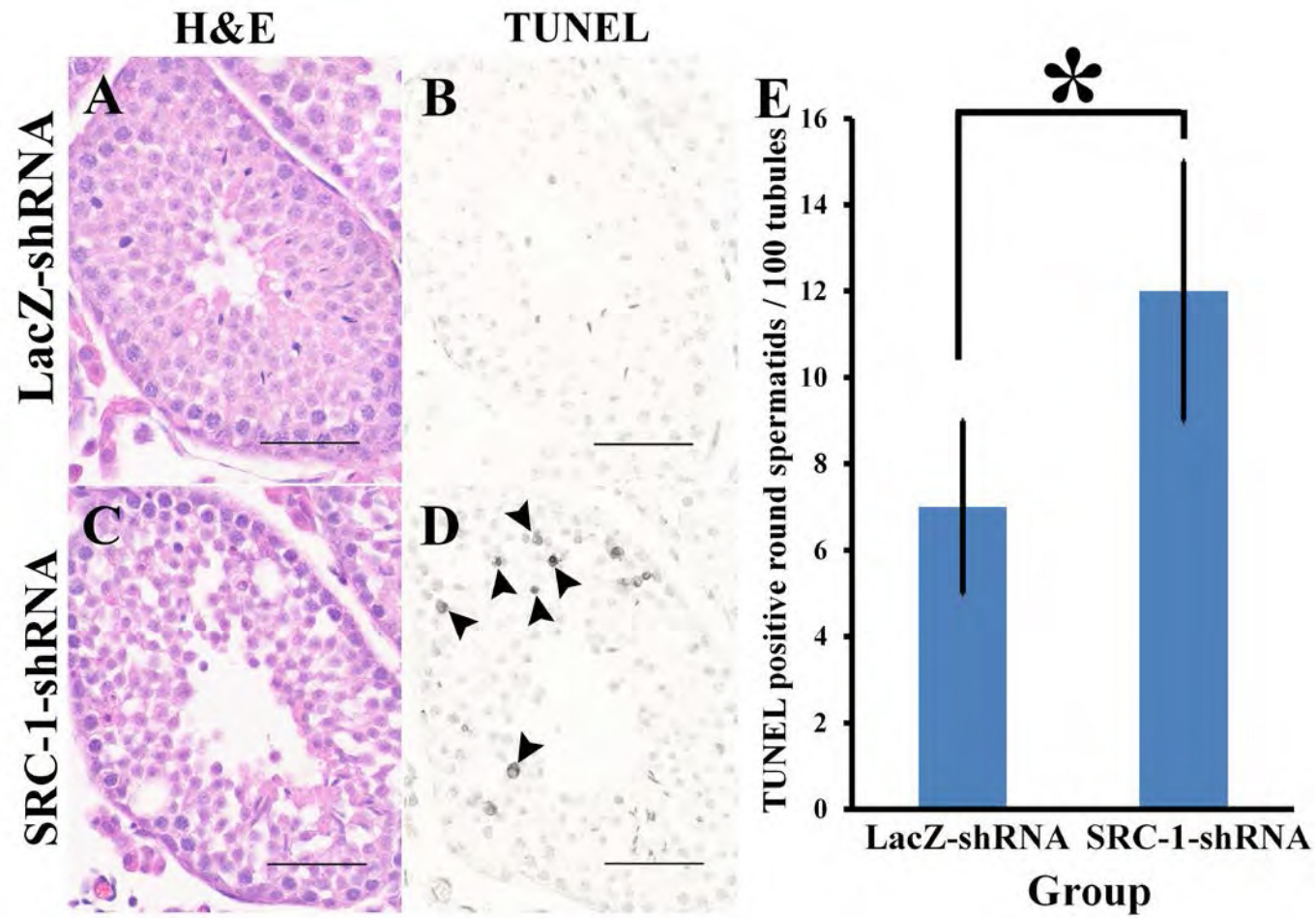


Fig. 11

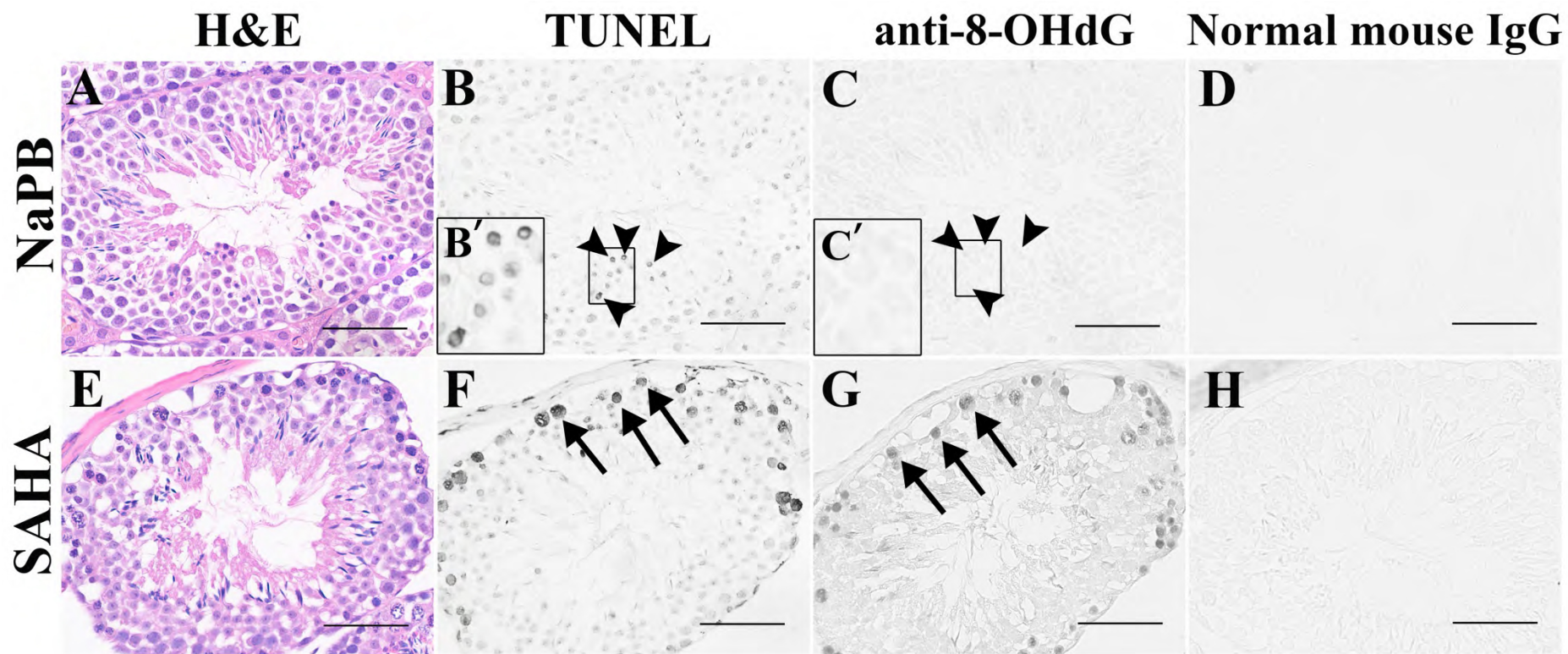


Fig. S1

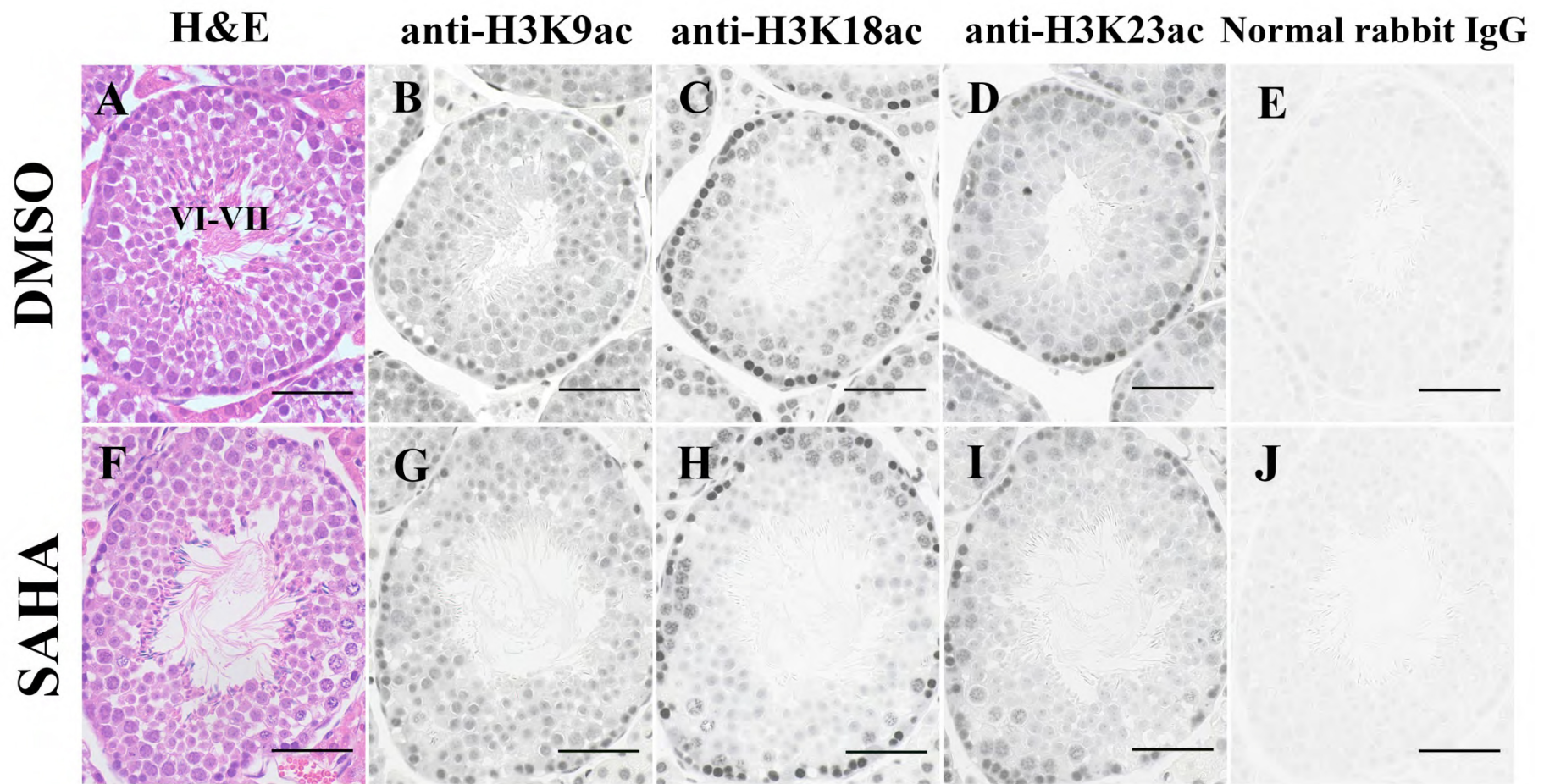


Fig. S2

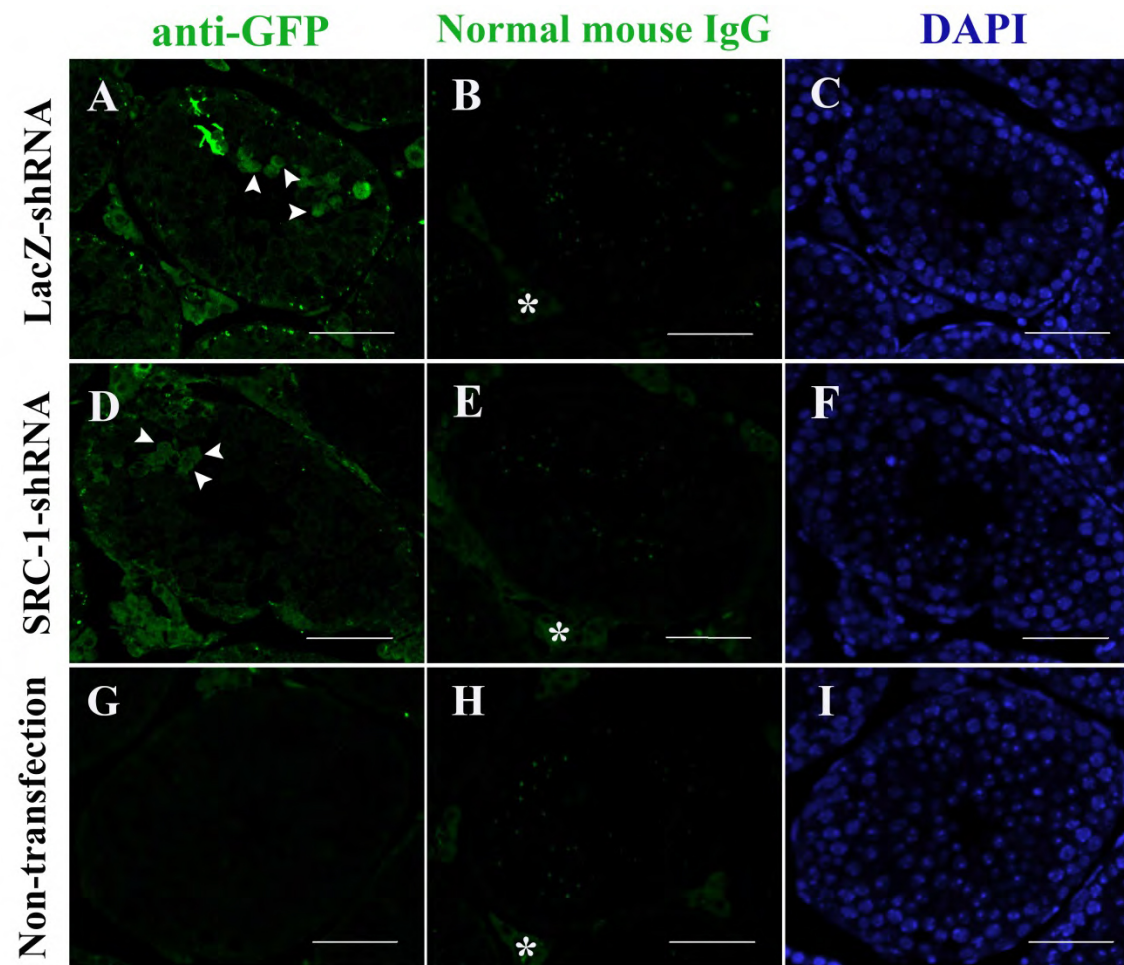


Fig. S3

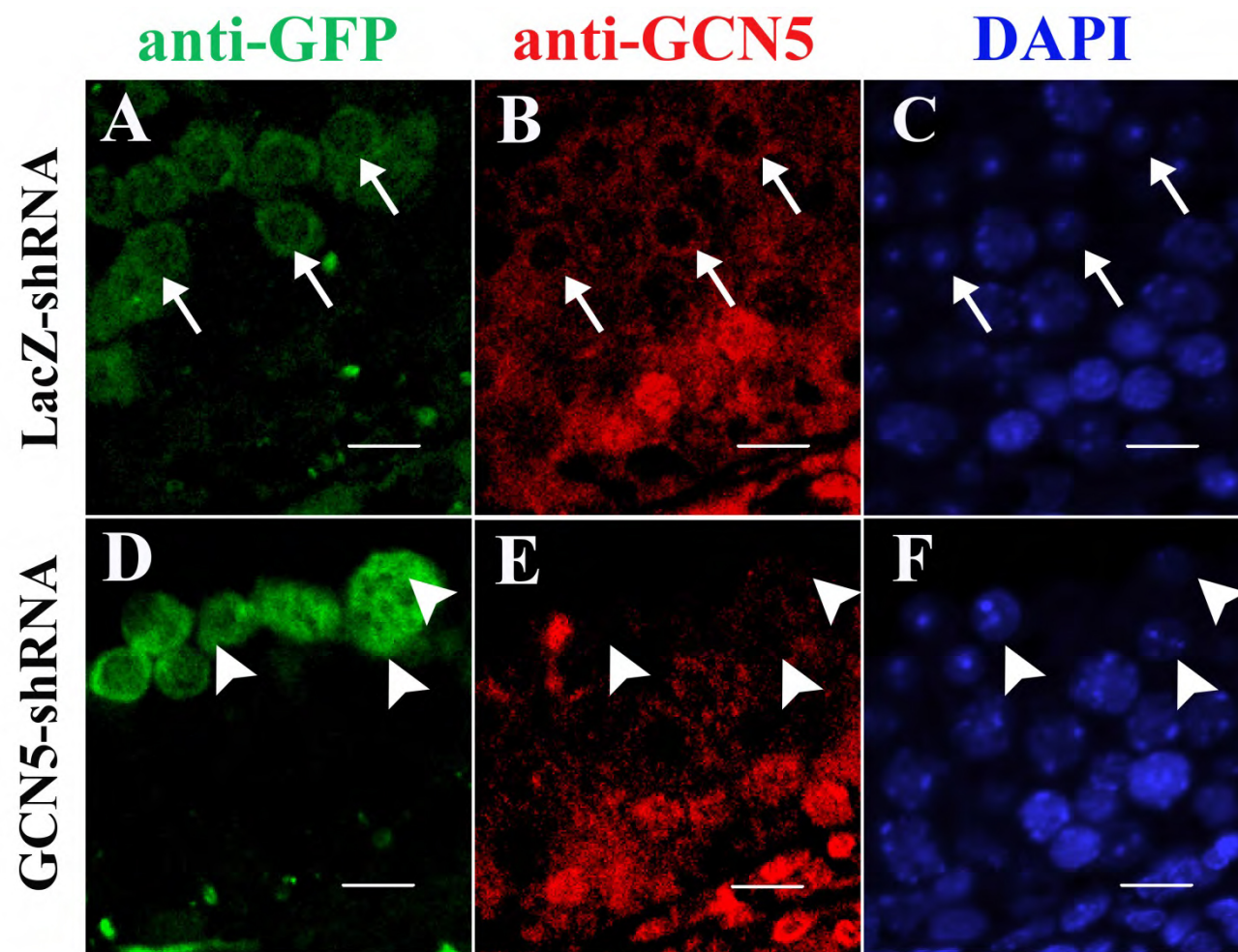


Fig. S4

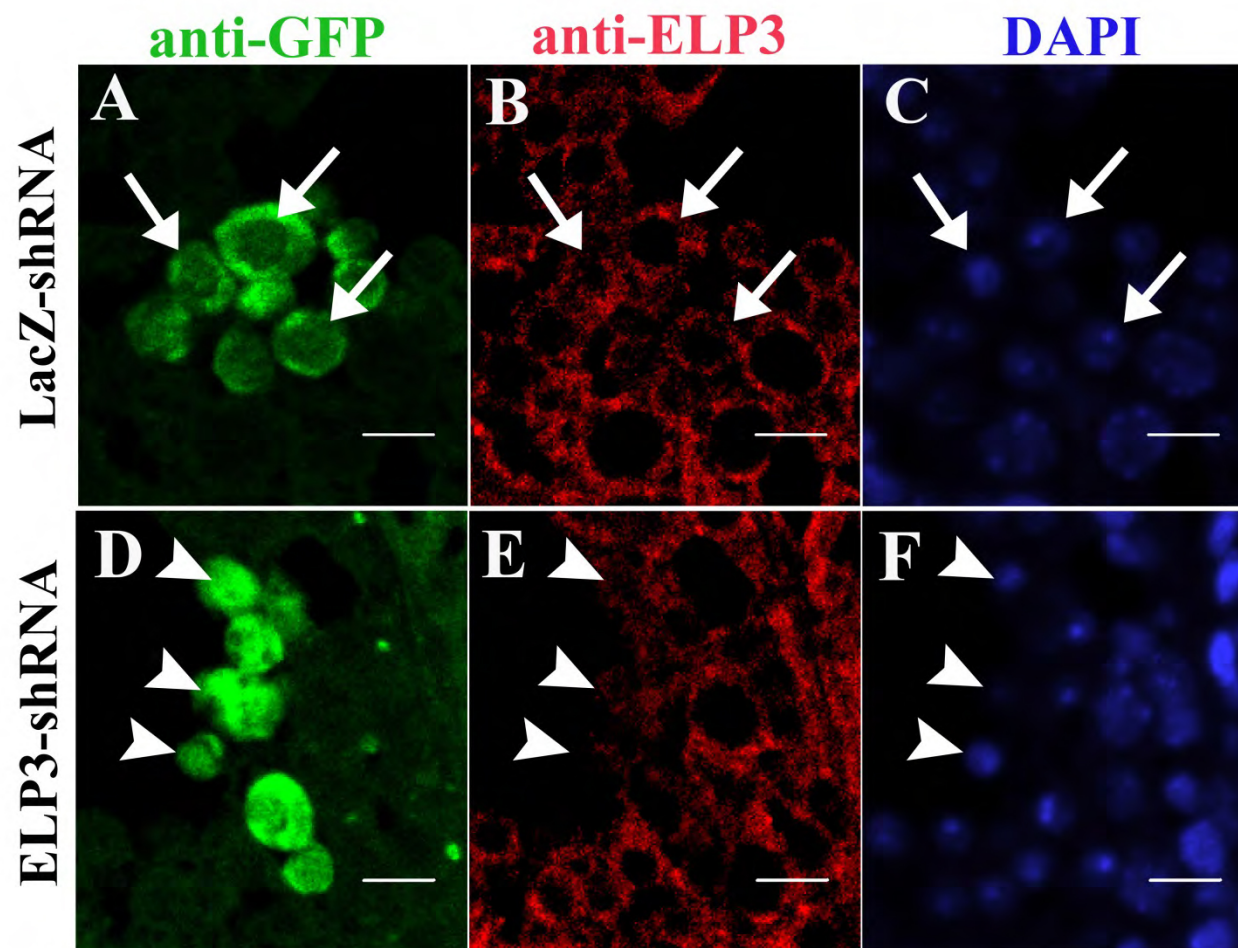


Fig. S5

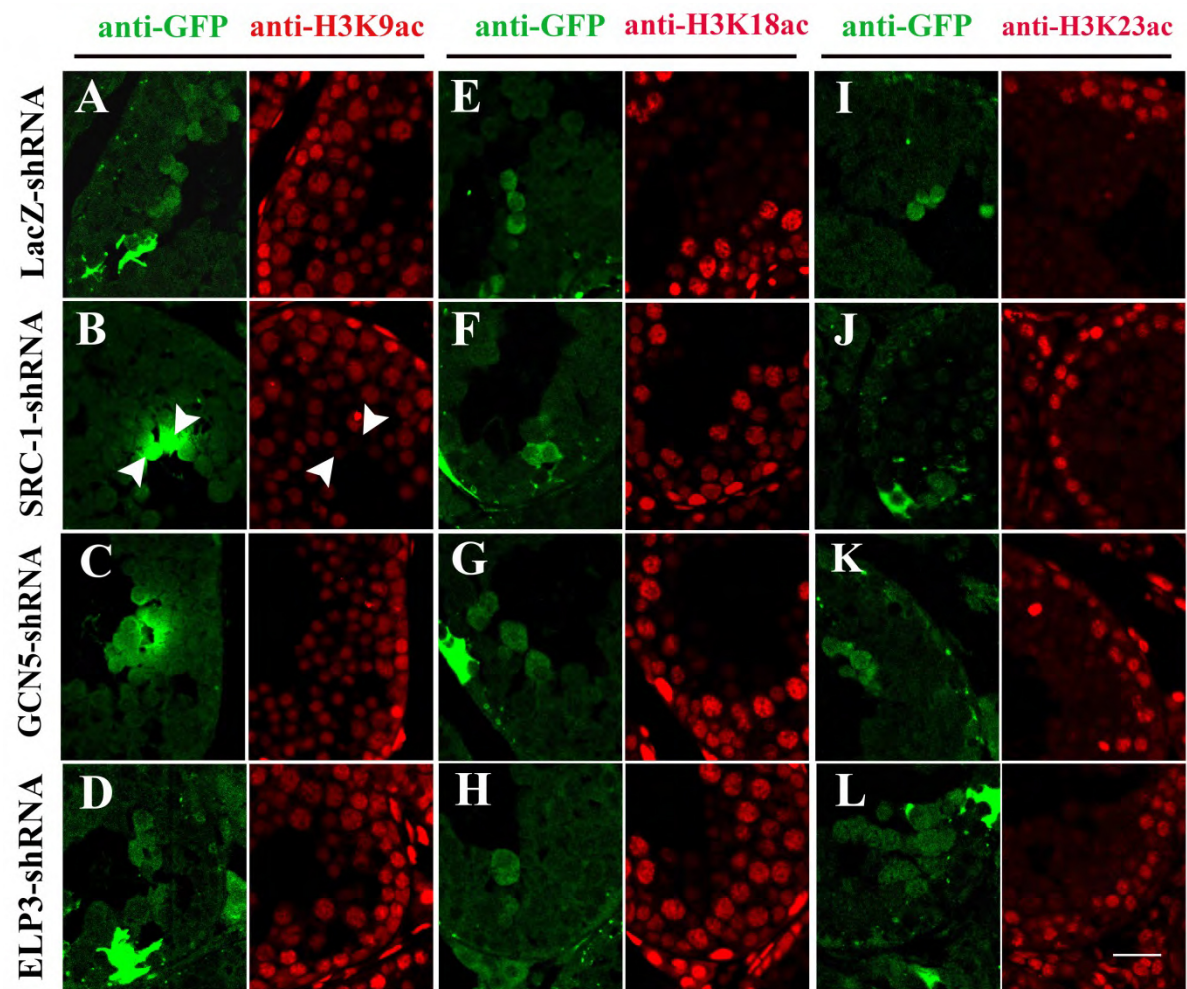


Fig. S6

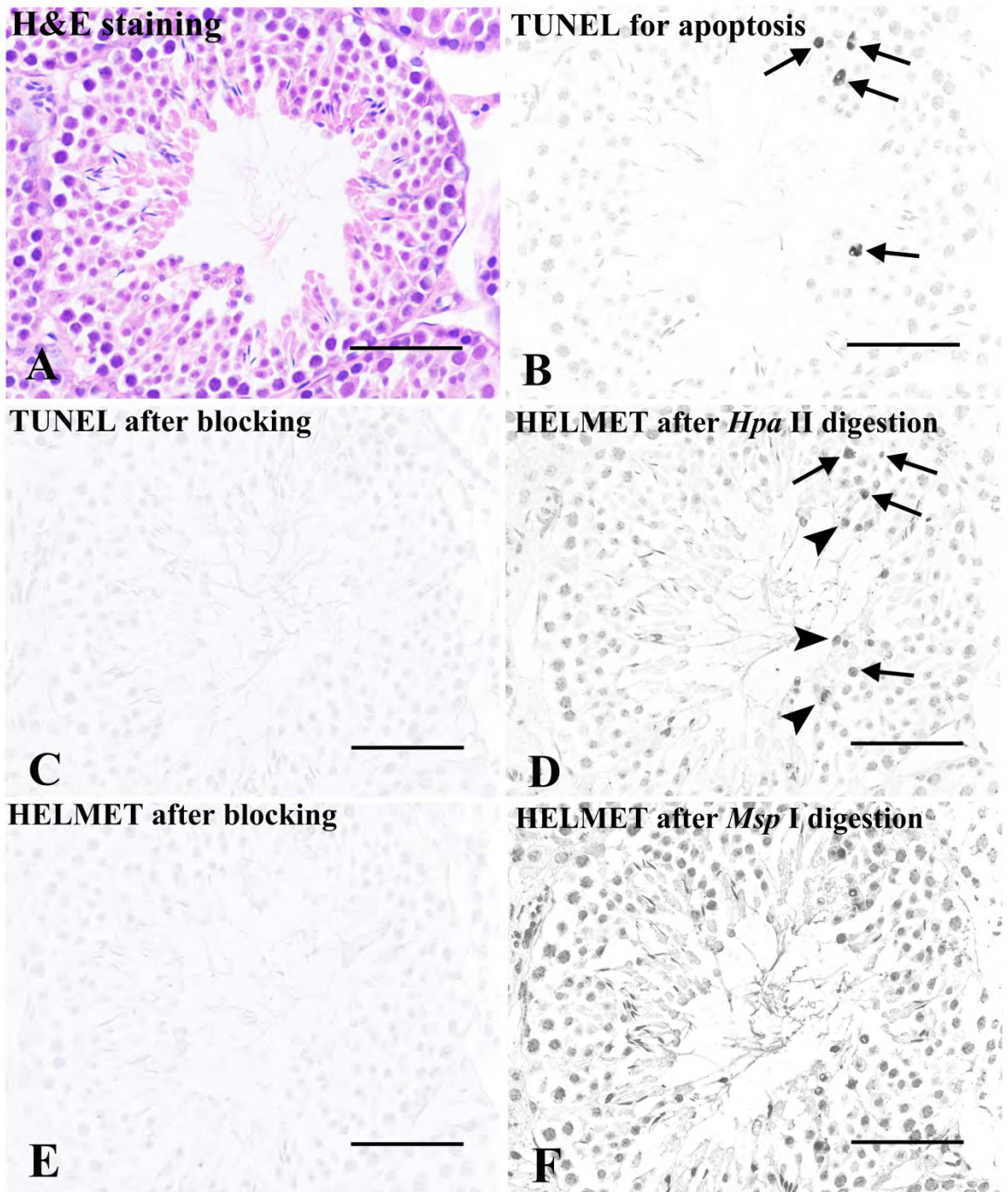


Fig. S7